6 Structure Functions

The main goal of this analysis is to measure $F_2(x,Q^2)$ and $xF_3(x,Q^2)$ and correct them to the partonic level, which are most directly related to the bare quark distributions. This Chapter describes the method of extracting the structure functions, the actual implementation of the method, and the studies of the systematic uncertainties. The resultant tables of structure functions, statistical errors, point-to-point systematic errors, and the physics-model corrections are given in Appendix D.

6.1 Method of Structure-Function Extraction

The extraction method follows from the definition of a differential cross-section in terms of the cross-section. The number of events in any *x* and Q^2 bin is given by:

$$N^{\nu,\bar{\nu}}(x,Q^2) = \rho L N_A \int_{x-bin} dx \int_{Q^2-bin} dQ^2 \int_{all\,energies} dE \frac{d\sigma^{\nu,\bar{\nu}}}{dx dQ^2} \Phi^{\nu,\bar{\nu}}(E) \tag{6.1}$$

where $\rho L N_A$ is the number of scattering centers in the target. Since this constant will be absorbed into the normalization constant $k^{\nu,\bar{\nu}}_{\Phi,POL}$ (Equation 6.20), it will be omitted from later equations for simplicity. Note that the integration runs over the bin limits in *x* and Q^2, but over the entire available energy spectrum in the range of the flux. The differential cross-section can be replaced with the general expression in terms of the structure functions:

$$\frac{d^2\sigma^{\nu,\bar{\nu}}}{dx dQ^2} = \frac{G^2 M}{\pi} \frac{E}{2MEx} \left[\left(1 - y - \frac{Mxy}{2E} \right) F_2 + \frac{y^2}{2} 2xF_1 \pm y\left(1 - \frac{y}{2} \right) xF_3 \right] \tag{6.2}$$

where the +(-) term corresponds to neutrinos(anti-neutrinos). (The factors in the first two fractions in Equation 6.2 have not been canceled because, within the analysis code, $G^2 M/\pi$ and $E\Phi$ are calculated separately.) The structure function $2xF_1$ is removed by using

$$2xF_1 = F_2 \frac{1+4M^2x^2/Q^2}{1+R} \tag{6.3}$$

where $R=\sigma_L/\sigma_T$, the ratio of the longitudinal to transverse cross-sections of the *W*-boson, is from a parameterization by Whitlow of the world's available data on the measurement of *R* [Whi90b]. This gives:

$$N^{\nu,\bar{\nu}}(x,Q^2) = \frac{G^2 M}{\pi}\int dx \int \frac{dQ^2}{2MEx}\int dE\, E\Phi^{\nu,\bar{\nu}}(E) \left[\left(1-y-\frac{Mxy}{2E}+\frac{y^2}{2}\frac{1+4M^2x^2/Q^2}{1+R(x,Q^2)}\right)F_2(x,Q^2) \pm y\left(1-\frac{y}{2}\right)xF_3(x,Q^2)\right] \tag{6.4}$$

The *x* and Q^2 bins are small enough that the structure functions do not vary significantly within each bin, and so they may be brought outside the integral. For each *x* and Q^2 bin there is a system of two linear equations in two unknowns to be solved for the structure function values in that bin:

$$N^{\nu}(x,Q^2) = A^{\nu}\ F_2(x,Q^2) + B^{\nu}\ xF_3(x,Q^2) \tag{6.5}$$

$$N^{\bar{\nu}}(x,Q^2) = A^{\bar{\nu}}\ F_2(x,Q^2) - B^{\bar{\nu}}\ xF_3(x,Q^2) \tag{6.6}$$

where

$$A^{\nu,\bar{\nu}} = \frac{G^2 M}{\pi}\iiint dx\frac{dQ^2}{2MEx}dE\,E\Phi^{\nu,\bar{\nu}}(E)\left(1-y-\frac{Mxy}{2E_\nu}+\frac{y^2}{2}\frac{1+4M^2x^2/Q^2}{1+R(x,Q^2)}\right) \tag{6.7}$$

$$B^{\nu,\bar{\nu}} = \frac{G^2 M}{\pi} \iiint dx \frac{dQ^2}{2MEx} dE\, E\Phi^{\nu,\bar{\nu}}(E) \left(y - \frac{y^2}{2} \right) \tag{6.8}$$

and $xF_3 = \left\langle xF_3^{\nu,\bar{\nu}} \right\rangle = \left(xF_3^{\nu} + xF_3^{\nu} \right) \Big/ 2$ (see Section 6.1.2). The solution of these equations is given by

$$\left.\begin{aligned} F_2(x,Q^2) &= \left(B^{\bar{\nu}} N^{\nu} + B^{\nu} N^{\bar{\nu}} \right) \Big/ \det \\ xF_3(x,Q^2) &= \left(A^{\bar{\nu}} N^{\nu} + A^{\nu} N^{\bar{\nu}} \right) \Big/ \det \\ \det &= A^{\nu} B^{\bar{\nu}} + B^{\nu} A^{\bar{\nu}} \end{aligned}\right\} \tag{6.9}$$

6.1.1 Error Calculation

Since the same event sums N^{ν} and $N^{\bar{\nu}}$ go into F_2 and xF_3, the two structure functions are correlated and there are three statistical errors: ΔF_2, ΔxF_3, and $\Delta F_2 \Delta xF_3$. The number of events that go into the calculation are corrected by the Monte Carlo as described in Section 4.1:

$$N_{corr}^{\nu,\bar{\nu}} = N_{meas}^{\nu,\bar{\nu}} \times \frac{MC_{GEN,no\,cuts}^{\nu,\bar{\nu}} \left(\text{with} \, 2\mu\sigma \right)}{MC_{SMR,SF\,cuts}^{\nu,\bar{\nu}} \left(\text{w/o} \, 2\mu\sigma \right)} \equiv N_{meas}^{\nu,\bar{\nu}} \times c_{MC}^{\nu,\bar{\nu}}(x,Q^2) \tag{6.10}$$

In calculating the statistical error on the structure functions, both the statistical error on the number of events and the statistical error in the Monte-Carlo correction must be considered. The error on the number of events $N_{meas}^{\nu,\bar{\nu}}$ is simple:

$$\left(\Delta N_{meas}^{\nu,\bar{\nu}} \right)^2 = N_{meas}^{\nu,\bar{\nu}} \tag{6.11}$$

However, the error on the Monte-Carlo correction has several components. Within a given (x,Q^2) bin the Monte Carlo events are being re-weighted and smeared; some

events leave the bin, others remain in the bin, and yet others enter the bin from other (x,Q^2) bins.

In order to calculate the statistical error on the Monte-Carlo correction $\Delta c_{MC}^{\nu,\bar{\nu}}(x,Q^2)$, the corrections were separately extracted for ten independent sets of Monte Carlo events. Each set of events was independently generated and smeared using a different random number seed. The statistical error was then taken to be the standard deviation of the resulting values of $c_{MC}^{\nu,\bar{\nu}}(x,Q^2)$.

The statistical errors ΔF_2, ΔxF_3, and $\Delta F_2 \Delta xF_3$ must then be calculated from Equations 6.9, 6.10, and the following:

$$\left(\Delta F_2\right)^2 = \sum_{i=\nu,\bar{\nu}} \left[\left(\frac{\partial F_2}{\partial N_{meas}^i} \right)^2 \left(\Delta N_{meas}^i \right)^2 + \left(\frac{\partial F_2}{\partial c_{MC}^i} \right)^2 \left(\Delta c_{MC}^i \right)^2 \right] \tag{6.12}$$

$$\left(\Delta xF_3\right)^2 = \sum_{i=\nu,\bar{\nu}} \left[\left(\frac{\partial xF_3}{\partial N_{meas}^i} \right)^2 \left(\Delta N_{meas}^i \right)^2 + \left(\frac{\partial xF_3}{\partial c_{MC}^i} \right)^2 \left(\Delta c_{MC}^i \right)^2 \right] \tag{6.13}$$

$$\Delta F_2 \Delta xF_3 = \sum_{i=\nu,\bar{\nu}} \left[\left(\frac{\partial F_2}{\partial N_{meas}^i} \right)\left(\frac{\partial xF_3}{\partial N_{meas}^i} \right)\left(\Delta N_{meas}^i \right)^2 + \left(\frac{\partial F_2}{\partial c_{MC}^i} \right)\left(\frac{\partial xF_3}{\partial c_{MC}^i} \right)\left(\Delta c_{MC}^i \right)^2 \right] \tag{6.14}$$

For simplicity, additional indices to represent the separate corrections required for focusing and defocusing events have been omitted from the above equations. The resulting expressions for the statistical errors are lengthy but straight-forward to calculate, and are incorporated into the structure-function extraction calculation.

6.1.2 Strange Sea Correction

In the leading-order parton model described in section 4.2, after the isoscalar corrections $F_2^{\nu} = F_2^{\bar{\nu}}$ but $xF_3^{\nu} \neq xF_3^{\bar{\nu}}$; that is, $xF_3^{\nu} - xF_3^{\bar{\nu}} = x(s-c)$, the difference between the strange- and charm-quark momentum sea densities in the proton. In the procedure derived from Equations 6.5-6.6, we extract $\langle xF_3 \rangle = \left(xF_3^{\nu} + xF_3^{\bar{\nu}} \right)/2 = x\left(u_v + d_v\right)$; that is, the effective xF_3 for both neutrinos and anti-neutrinos is the sum of the valence up- and down-quark momentum distributions in the proton. In order for the physics-model corrections to apply to this procedure, there must be an additional correction applied to the formula in Equation 4.13:

$$corr^{\,strange-sea} = \frac{\sigma\left(xF_3^{\nu} = xF_3^{\bar{\nu}} = \langle xF_3 \rangle \right)}{\sigma\left(xF_3^{\nu} - xF_3^{\bar{\nu}} = x(s-c) \right)} \tag{6.15}$$

The physics model of section 4.2 assumes the charm quark distribution is zero [Mis89]. The strange sea is measured in studies of dimuon production in neutrino interactions; in this analysis the leading-order result from the E744 and E770 data is used [Rab92].† The measurements find the level of the strange sea to be about 1/3rd that of the non-strange sea, and the x-distribution to be more sharply peaked. These differences are parameterized by κ and α defined by:

$$\int xs\,dx = \int x\bar{s}\,dx = \kappa \int \left(x\bar{u} + x\bar{d} \right)/2\,dx \tag{6.16}$$

$$xs = x\bar{s} \propto \frac{\left(x\bar{u} + x\bar{d} \right)}{2}(1-x)^{\alpha} \tag{6.17}$$

---

† The next-to-leading-order result of [Baz95] is not appropriate for the leading-order physics model.

with $\kappa = 0.373$ and $\alpha = 2.50$.

6.1.3 Large-*x* Events and the Monte Carlo

In the physics model described in section 4.2, the parton distributions used to generate the Monte Carlo approach zero as $x \to 1$. After the Monte-Carlo and physics-model corrections are applied to the data, the corrected data distributions are therefore forced to go to zero as $x \to 1$. Thus, with this model, a structure function measurement for $x \sim 1$ cannot be made.

On the other hand, the structure functions in iron should *not* vanish at $x = 1$. Effects such as Fermi motion give a non-zero contribution for $x > 1$. Studies of Fermi motion indicate that the corrections to the structure-functions are less than 5% for $x < 0.55$, about 20% at $x = 0.65$, and about 40% at $x = 0.75$ [Bod81]. No Fermi-motion corrections have been made in this structure-function extraction since, at the values of x for which they would be important, the statistical errors, systematic errors, and smearing corrections are so large that this large-x data would be excluded from this analysis by the standard analytic cuts.

A separate issue at large (and small) x is the amount of smearing between x-bins. The x-distributions are steeply falling at high x. This implies that the events from lower x-bins smear into higher ones leading to large smearing corrections. This issue is addressed by the histograms in Figures 6.1 through 6.5. These plots show the distribution of x-reconstructed, x_{REC}, in bins of x-generated, x_{GEN}, from the Monte Carlo. These distributions show that in the x-bins chosen for this analysis, enough reconstructed events remain in the bin in which they were generated for the measurement of the structure functions to be meaningful.

It is interesting to note that roughly twice as many uncorrected data events with $x > 1$ are observed in the data as are generated by our Monte Carlo after resolution-smearing effects have been applied. Others in the collaboration are studying the possibility of whether this is due to radiative corrections or Fermi-motion corrections for these events.

6.1.4 Alternate Extraction Methods

There are other methods of extracting F_2 and xF_3, and the collaboration is presently exploring such methods. One alternative is to go back to the expression for the differential cross-section:

$$\frac{d^2\sigma^{\nu,\bar{\nu}}}{dxdy} = \frac{G^2 ME}{\pi}\left[\left(1 - y - \frac{Mxy}{2E}\right)F_2 + \frac{y^2}{2}2xF_1 \pm y\left(1 - \frac{y}{2}\right)xF_3\right] \tag{6.10}$$

If one extracted the cross-sections $d^2\sigma/dxdy$, the structure functions could be determined by fitting to the *y*-distribution of the cross-sections within each (x, Q^2) bin. In a related analysis, Un-Ki Yang is using a similar technique to determine *R* from the E744 and E770 neutrino data.

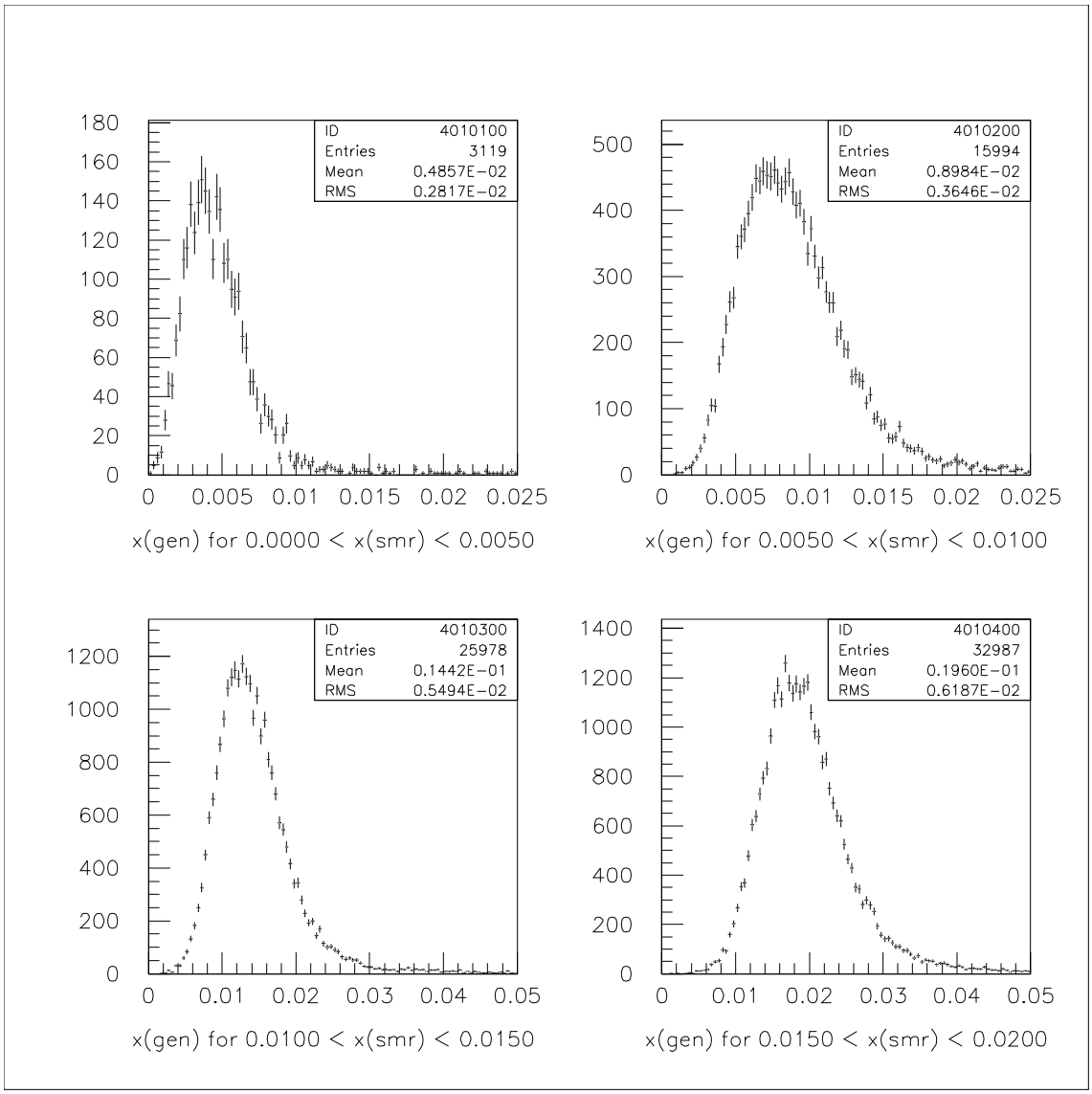

Figure 6.1: x_{GEN} for $0 < x_{SMR} < 0.02$. These plots show that for:

.000 < $x_{observed}$ < 0.005, 54% of the events are generated within the bin;

.005 < $x_{observed}$ < 0.010, 51% of the events are generated within the bin;

.010 < $x_{observed}$ < 0.015, 41% of the events are generated within the bin;

.015 < $x_{observed}$ < 0.020, 34% of the events are generated within the bin.

The first bin in this figure is not included in the structure-function analysis due to poor statistics and large systematic errors.

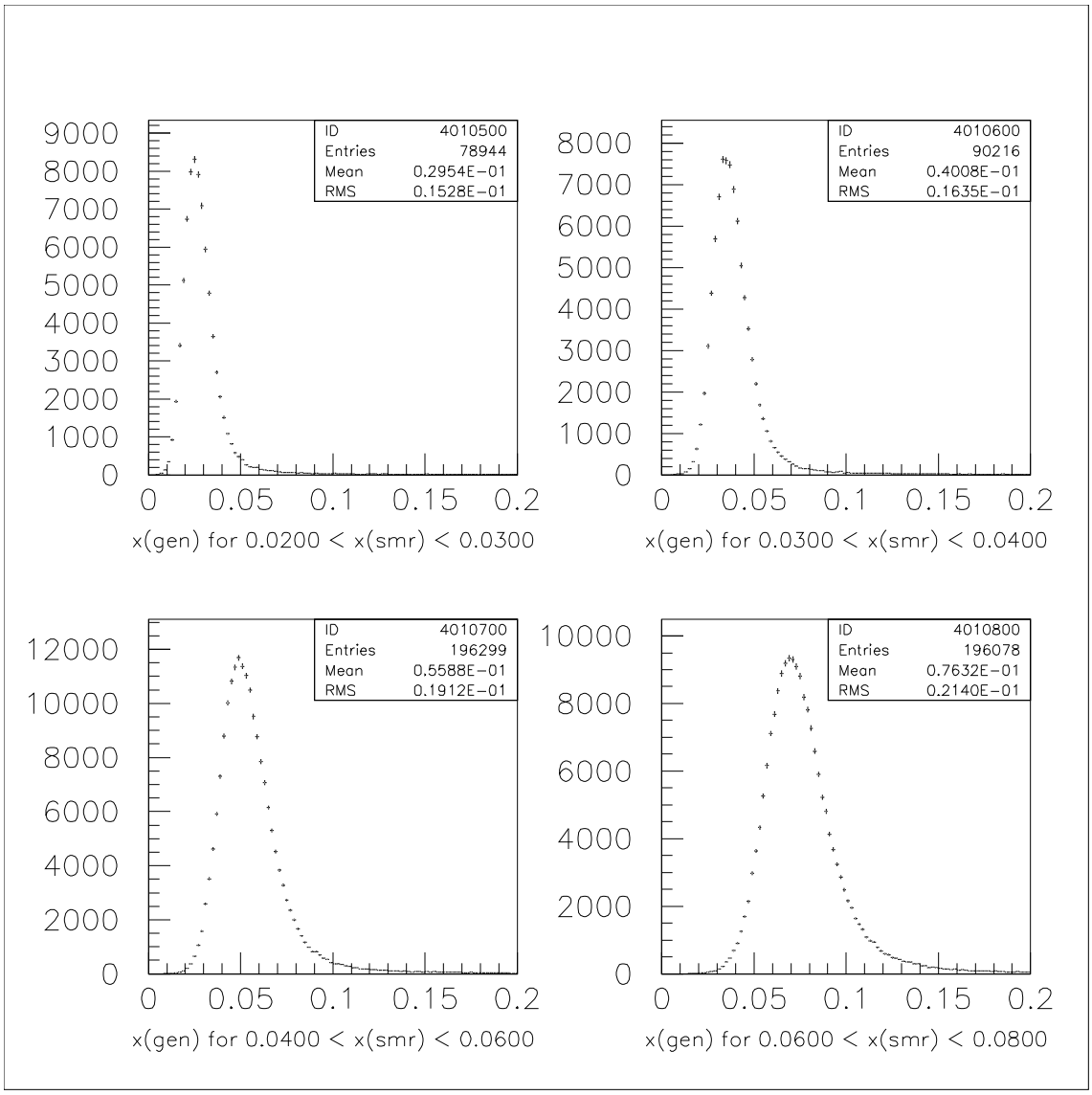

Figure 6.2: x_{GEN} for 0.02 < x_{SMR} < 0.08. These plots show that for:

.02 < $x_{observed}$ < 0.03, 48% of the events are generated within the bin;

.03 < $x_{observed}$ < 0.04, 40% of the events are generated within the bin;

.04 < $x_{observed}$ < 0.06, 54% of the events are generated within the bin;

.06 < $x_{observed}$ < 0.08, 45% of the events are generated within the bin.

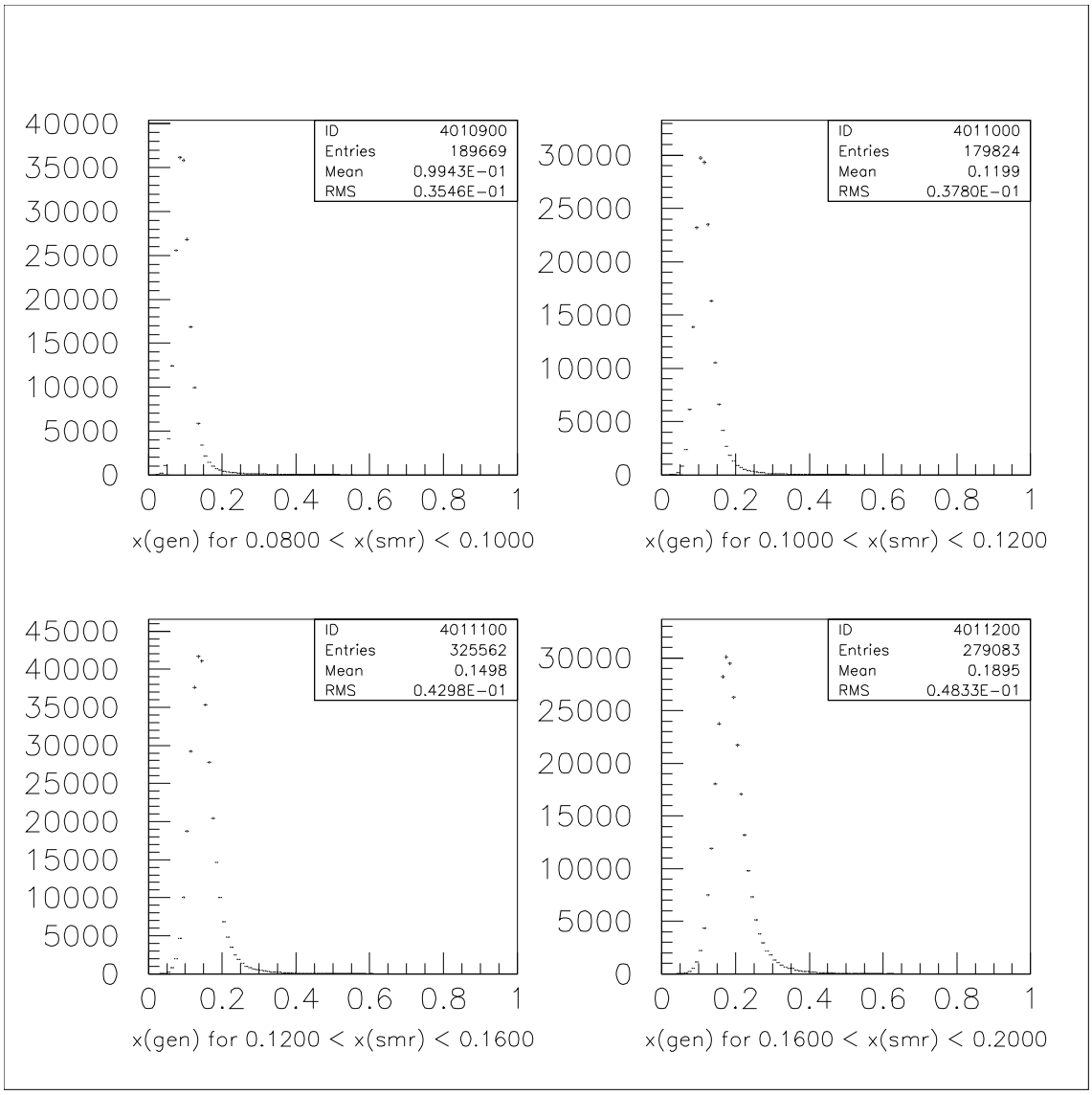

Figure 6.3: x_{GEN} for 0.08 < x_{SMR} < 0.20. These plots show that for:

.08 < $x_{observed}$ < 0.10, 38% of the events are generated within the bin;

.10 < $x_{observed}$ < 0.12, 30% of the events are generated within the bin;

.12 < $x_{observed}$ < 0.16, 48% of the events are generated within the bin;

.16 < $x_{observed}$ < 0.20, 41% of the events are generated within the bin.

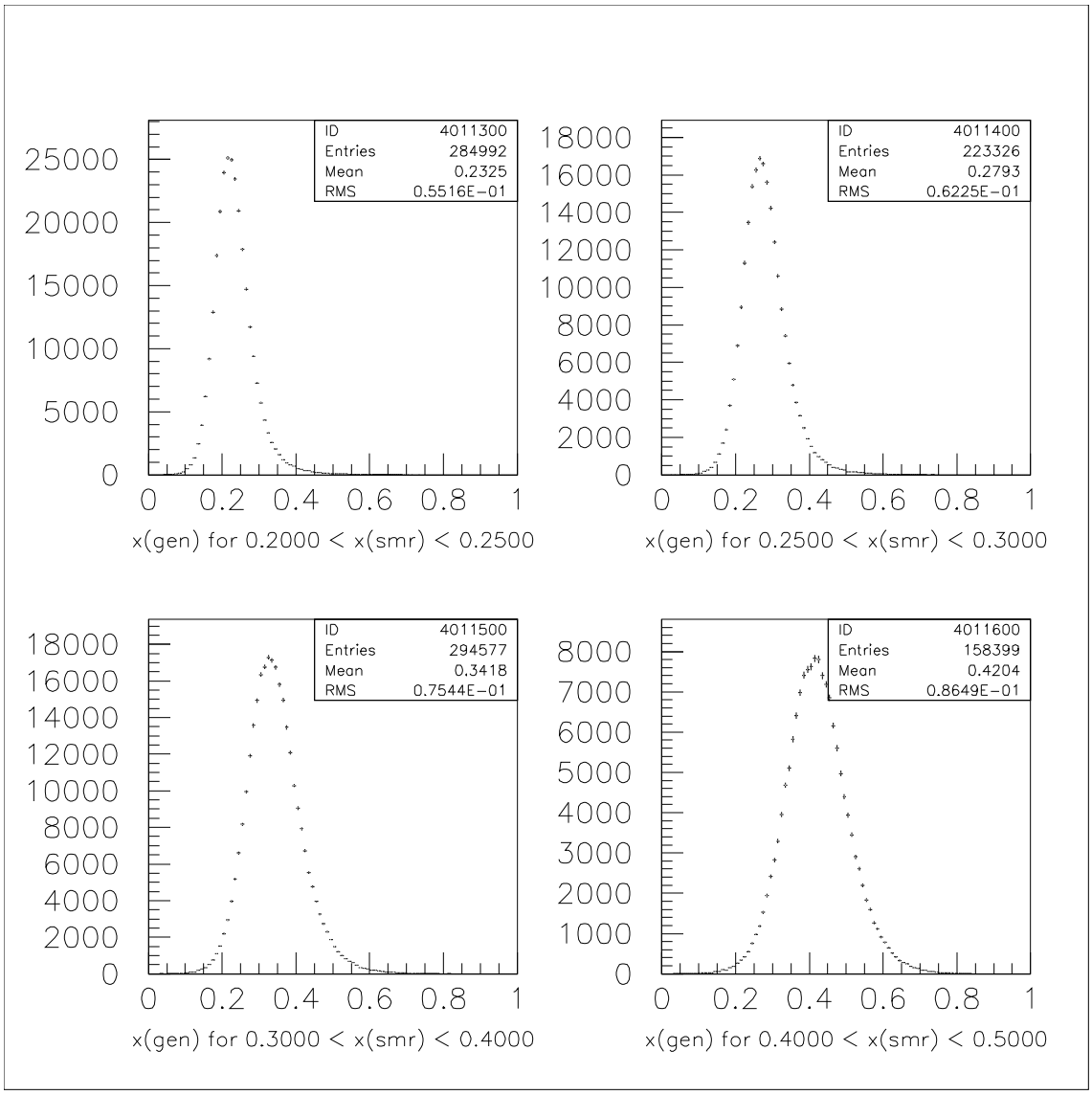

Figure 6.4: x_{GEN} for 0.20 < x_{SMR} < 0.50. These plots show that for:

.20 < $x_{observed}$ < 0.25, 42% of the events are generated within the bin;

.25 < $x_{observed}$ < 0.30, 36% of the events are generated within the bin;

.30 < $x_{observed}$ < 0.40, 52% of the events are generated within the bin;

.40 < $x_{observed}$ < 0.50, 42% of the events are generated within the bin.

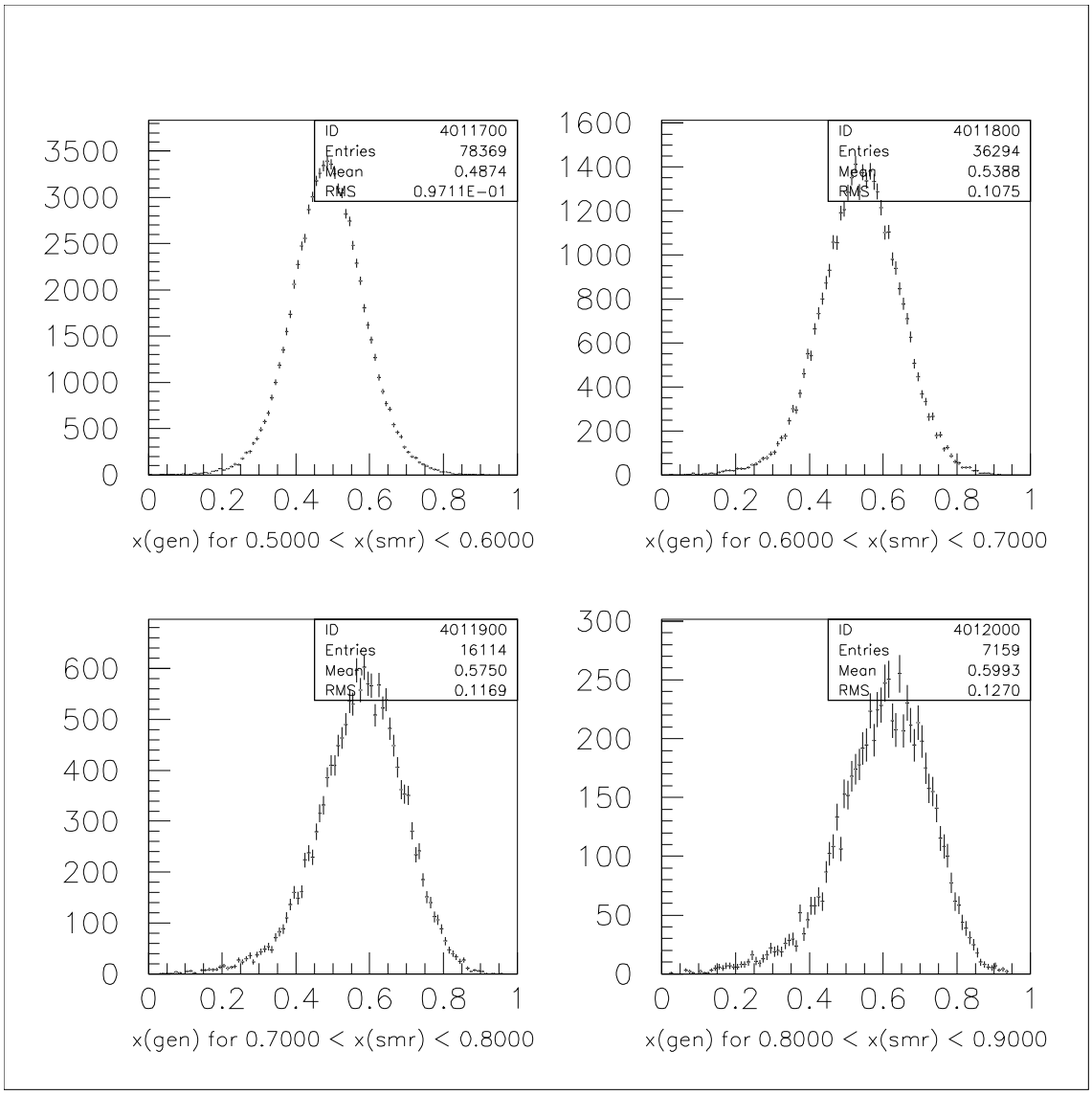

Figure 6.5: x_{GEN} for $0.5 < x_{SMR} < 0.9$. These plots show that for:

$.5 < x_{observed} < 0.6$, 32% of the events are generated within the bin;

$.6 < x_{observed} < 0.7$, 22% of the events are generated within the bin;

$.7 < x_{observed} < 0.8$, 12% of the events are generated within the bin;

$.8 < x_{observed} < 0.9$, 3% of the events are generated within the bin.

Due to the large amount of smearing for $x > 0.8$, these data are not included in the structure-function analysis. The structure functions for $0.7 < x < 0.8$ are reported in this thesis, but they are not included in the QCD fits of Chapter 7.

Another method is to multiply both sides of Equation 6.10 by the flux, integrate over the (x,Q^2) bin and over all energies, and to consider neutrinos and anti-neutrinos separately:

$$N^{\nu}(x,Q^2) \propto \iiint dx \frac{dQ^2}{2MEx} E\Phi^{\nu}(E)dE \left[\left(1 - y - \frac{Mxy}{2E}\right)F_2 + \frac{y^2}{2} 2\,xF_1 + y\left(1 - \frac{y}{2}\right)xF_3^{\nu} \right] \tag{6.11}$$

$$N^{\bar{\nu}}(x,Q^2) \propto \iiint dx \frac{dQ^2}{2MEx} EdE\Phi^{\bar{\nu}}(E) \left[\left(1 - y - \frac{Mxy}{2E}\right)F_2 + \frac{y^2}{2} 2\,xF_1 - y\left(1 - \frac{y}{2}\right)xF_3^{\bar{\nu}} \right] \tag{6.12}$$

Since $F_2^{\nu} = F_2^{\bar{\nu}}$ and $2xF_1^{\nu} = 2xF_1^{\bar{\nu}}$, only the difference between xF_3^{ν} and $xF_3^{\bar{\nu}}$ need be considered. By doing fits to the *y*-distributions within the (x,Q^2) bin, the values of F_2, $2xF_1$, xF_3^{ν}, and $xF_3^{\bar{\nu}}$ can be determined. From the relation in Equation 6.3 R can be determined; from the difference between xF_3^{ν} and $xF_3^{\bar{\nu}}$, one can determine *s*-*c*, the difference between the strange and charm quark distributions. Cindy McNulty is working on this analysis.

6.2 Implementing the Method

This section describes the implementation the structure-function calculation described above. The program code used to perform the calculation is in Appendix B.

6.2.1 Structure-Function Cuts

The data events are binned in 16 Q^2 bins and 18 *x* bins. The bins cover the entire *x* range from 0 to 1, and the Q^2 range from 1 to 600 GeV. In addition to fiducial volume and acceptance cuts discussed in chapter 3, the following cuts are applied:

• $30\,GeV < E_\nu < 360\,GeV$ — The lower limit of 30 GeV was selected because the lower energy bins in the flux analysis have a large systematic error. The upper limit of 360 GeV was picked because above that energy the error on the Monte-Carlo smearing corrections becomes large; also, the number of anti-neutrino events above 360 GeV is small and hence a coupled analysis with neutrino data cannot be made.

• $\theta_\mu < 150\,mr$ — This cut assures good acceptance of the muon track as it passes through the muon spectrometer.

• $E_{HAD} > 10\,GeV$ — This lower limit on E_{HAD} was picked to minimize the correlations between the flux and structure-function data sample (see Chapter 5).

• $E_\mu > 15\,GeV$ — 15 GeV is the lower limit of acceptance of the muon spectrometer.

• $Q^2 > 1\,GeV^2$ — This eliminates the quasi-elastic events from the data sample, which are not modeled in our Monte Carlo. An analysis is being prepared by the collaboration to determine the structure functions for $Q^2 < 1\,GeV^2$.

6.2.2 Structure-Function Calculation

As in the flux extraction, events and corrections must be binned in separate categories: the two experiments E744 and E770, neutrinos and anti-neutrinos, and the muon

Table 6.1: Number of events passing structure-function cuts.

	E744				E770			
Neutrino Type	ν	ν	$\bar{\nu}$	$\bar{\nu}$	ν	ν	$\bar{\nu}$	$\bar{\nu}$
Toroid Pol	Foc μ^-	Foc μ^+	Foc μ^-	Foc μ^+	Foc μ^-	Foc μ^+	Foc μ^-	Foc μ^+
Raw Events	700579	682503	97111	101451	798445	845644	116657	133188
Fid. Volume	442935	508164	59459	73880	592267	625309	88821	99825
Geometric	282796	284111	48150	64182	377318	345351	71986	86957
$\theta_\mu < 150\,mr$	280262	283833	48134	64018	373955	345062	71961	86735
$E_\mu > 15\,GeV$	276420	283205	48002	63077	368889	344366	71807	85383
$E_{HAD} > 10$	227607	230696	32766	43444	305657	282161	48421	58285
$Q^2 > 1\,GeV^2$	219772	222444	30624	40751	295495	272179	45177	54607
$30 < E < 360$	207630	209050	30226	40276	278552	255330	44637	53975

spectrometer set to focusing positively- or negatively-charged muons. This gives a total of eight categories (two experiments × two neutrino species × two spectrometer settings.) The number of events passing each of these cuts in each category is given in Table 6.1.

A total of 950562 neutrino and 169114 anti-neutrino events pass the structure-function cuts. The structure functions are determined separately for E744 and E770 as follows. For each (x, Q^2) bin, Equations 6.5 and 6.6 are implemented by:

$$\left(DA^{\nu,\bar{\nu}}_{ACC,FOC} \times allcorr^{\nu,\bar{\nu}}_{FOC} + DA^{\nu,\bar{\nu}}_{ACC,DEF} \times allcorr^{\nu,\bar{\nu}}_{DEF}\right)_{x,Q^2} = A^{\nu,\bar{\nu}} F_2(x,Q^2) \pm B^{\nu,\bar{\nu}} xF_3(x,Q^2) \tag{6.18}$$

where $DA^{\nu,\bar{\nu}}_{ACC,FOC}$ ($DA^{\nu,\bar{\nu}}_{ACC,DEF}$) are the *uncorrected* number of data events that pass all cuts for the spectrometer set to focus (defocus) negatively-charged muons, $A^{\nu,\bar{\nu}}$ and $B^{\nu,\bar{\nu}}$ are defined in Equations 6.7 and 6.8 above, and *allcorr* is the total correction that must be applied to the data events within each category, and for each (x,Q^2) bin. It is defined by

$$allcorr^{\nu,\bar{\nu}}_{POL}(x,Q^2) = \frac{corr^{\nu,\bar{\nu}}_{overall,POL}(x,Q^2)}{k^{\nu,\bar{\nu}}_{\Phi,POL}} \tag{6.19}$$

for *POL = FOC, DEF* (that is, *allcorr* is calculated separately for toroid focusing (defocusing) negatively-charged muons), and for neutrinos and anti-neutrinos. $k^{\nu,\bar{\nu}}_{\Phi,POL}$ is the normalization between the flux extracted by the fixed-ν method and $\sigma^{\nu,\bar{\nu}}_{world}$, the world average ν-Fe isoscalar-corrected cross-section (as noted in Section 5.3, the fixed-ν method cannot determine the absolute normalization of the flux). $k^{\nu,\bar{\nu}}_{\Phi,POL}$ also absorbs ρLN_A from Equation 6.1 and is calculated from the following relation:

$$\begin{aligned} & DA^{\nu,\bar{\nu}}_{cuts,POL} \times \frac{MC^{\nu,\bar{\nu}}_{GEN,POL}}{MC^{\nu,\bar{\nu}}_{SMR,cuts,POL}} \\ & = \underbrace{k^{\nu,\bar{\nu}}_{\Phi,POL}\,\frac{\sigma^{\nu,\bar{\nu}}_{world}}{E}\int_{30}^{200} dE\; E\Phi^{\nu,\bar{\nu}}(E)}_{Factor\ 1} \times \underbrace{\frac{\left(\int dE\,\frac{\sigma^{\nu,\bar{\nu}}_{model,Fe}}{E}E\Phi^{\nu,\bar{\nu}} \Big/ \int dE\,E\Phi^{\nu,\bar{\nu}}\right)}{\left(\int dE\,\frac{\sigma^{\nu,\bar{\nu}}_{model,iso}}{E} \Big/ \int dE\right)}}_{Factor\ 2} \end{aligned} \tag{6.20}$$

The left-hand side of Equation 6.20 computes the number of data events seen in the analysis and applies the Monte-Carlo correction, where "cuts" refers to the cross-section analysis cuts described in Section 3.3.3. Factor 1 of the right-hand side computes the number of events predicted in this experiment from the world-average isoscalar cross-

section. Factor 2 computes the correction from the number of events predicted for an isoscalar target to the number of events predicted for an Fe target, where the physics model used is the one described in Section 4.2. Note that the denominator of Factor 2 computes the energy-weighted average of the isoscalar cross-section predicted by the model which corresponds to the world-average cross-section in Factor 1, but the numerator of Factor 2 computes the flux×energy-weighted average of the model's Fe cross-section which corresponds to the quantity on the left-hand side of the equation. All energy integrals in Equation 6.20 are computed over the range 30-200 *GeV,* because the world-average cross-section was determined for that energy range.

Returning to the definition of *allcorr* in Equation 6.19, the term $corr_{overall}$ is the bin-by-bin acceptance, smearing, model, and bin-center corrections applied to the data. It is calculated by

$$corr^{\nu,\bar{\nu}}_{overall,POL}(x,Q^2) = \frac{n^{\nu,\bar{\nu}}_{bin-center}\left(\text{with}\,2\mu\right)}{MC^{\nu,\bar{\nu}}_{SMR,SF-cuts,POL}\left(\text{no}\,2\mu\right)} \tag{6.21}$$

where *SF-cuts* refers to the structure-function analysis cuts described above, and $n^{\nu,\bar{\nu}}_{bin-center}$ is the number of events predicted by the Monte Carlo, corrected for the physic-model corrections and the bin-center correction described in chapter 4, and the strange-sea correction described in section 6.1.2. Instead of applying an overall bin correction to determine $n^{\nu,\bar{\nu}}_{bin-center}$, as implied by Equation 4.1, $n^{\nu,\bar{\nu}}_{bin-center}$ is determined by re-weighting the Monte Carlo:

$$n^{\nu,\bar{\nu}}_{bin-center} = \sum_{\substack{Gen\,MC\,events\\ in(x,Q^2)bin}} \frac{\sigma^{\nu,\bar{\nu}}_{bare}(x_{BC},y_{BC},E_{gen})}{\sigma^{\nu,\bar{\nu}}_{phys}(x_{gen},y_{gen},E_{gen})} \tag{6.22}$$

where $\sigma_{bare}^{\nu,\bar{\nu}}$ is computed assuming an isoscalar target of bare quarks with no radiative, charm-mass, or *W*-boson propagator effects, and with $xF_3 = \left\langle xF_3^{\nu,\bar{\nu}} \right\rangle$. This method of calculating the physics-model corrections is more robust than the correction of Equation 4.1, since it properly averages the correction given the underlying kinematic distribution within the (x, Q^2) bin.

Figure 6.6 displays $corr_{overall}$ for neutrino events; Figure 6.7 displays $corr_{overall}$ for anti-neutrino events. The subsequent figures display some of the individual correction factors that are part of $corr_{overall}$: Figures 6.8-6.9 display the acceptance correction; Figures 6.10-6.11 display the smearing correction; Figure 6.12-6.13 display the physics-model correction; Figures 6.14-6.15 display the bin-center correction. As can be seen in the plots, the largest component of $corr_{overall}$ comes from the acceptance correction, which is the correction from applying the structure-function cuts to the reconstructed events.

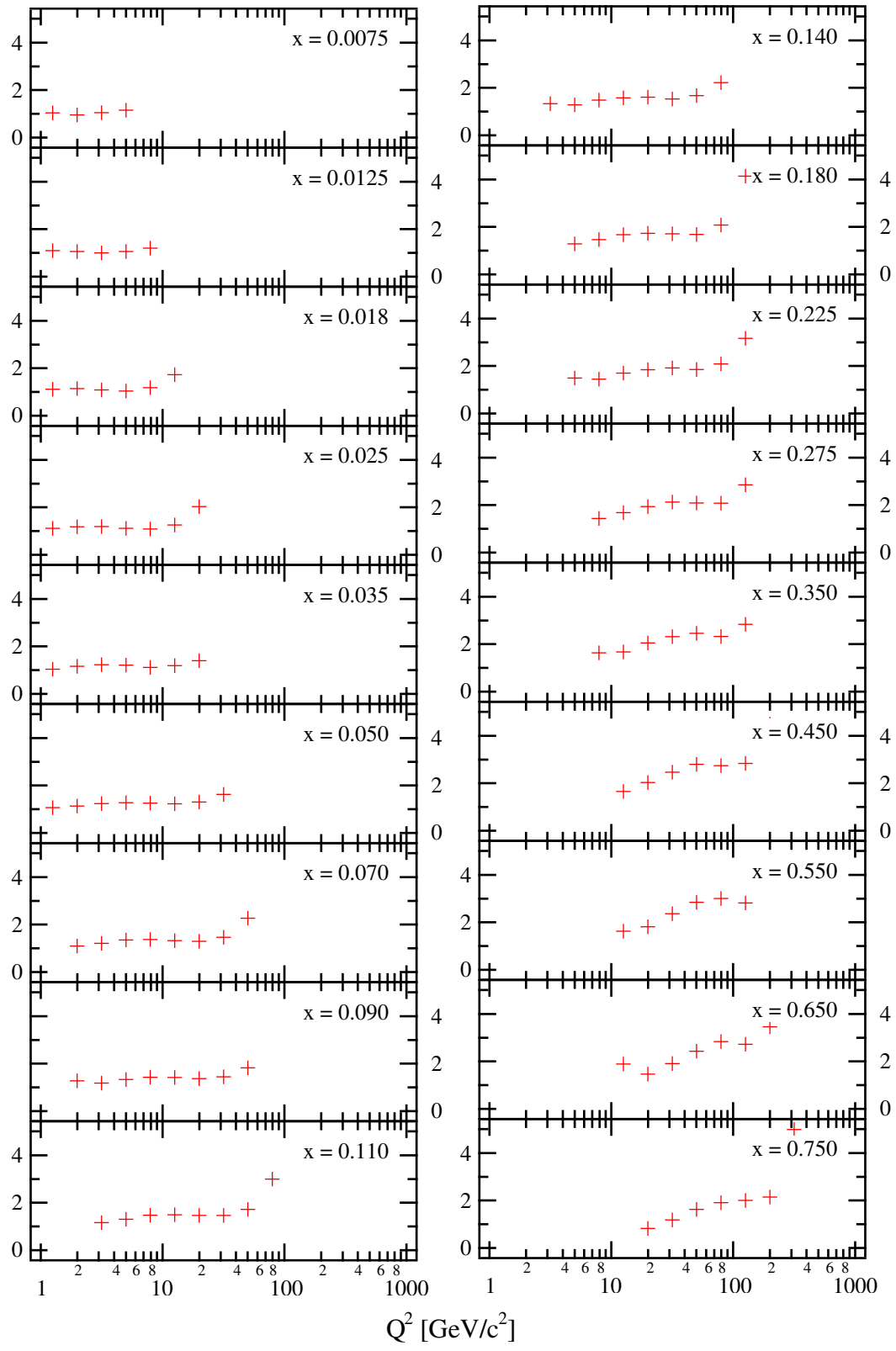

Figure 6.6: The total corrections applied to neutrino events in the structure-function analysis.

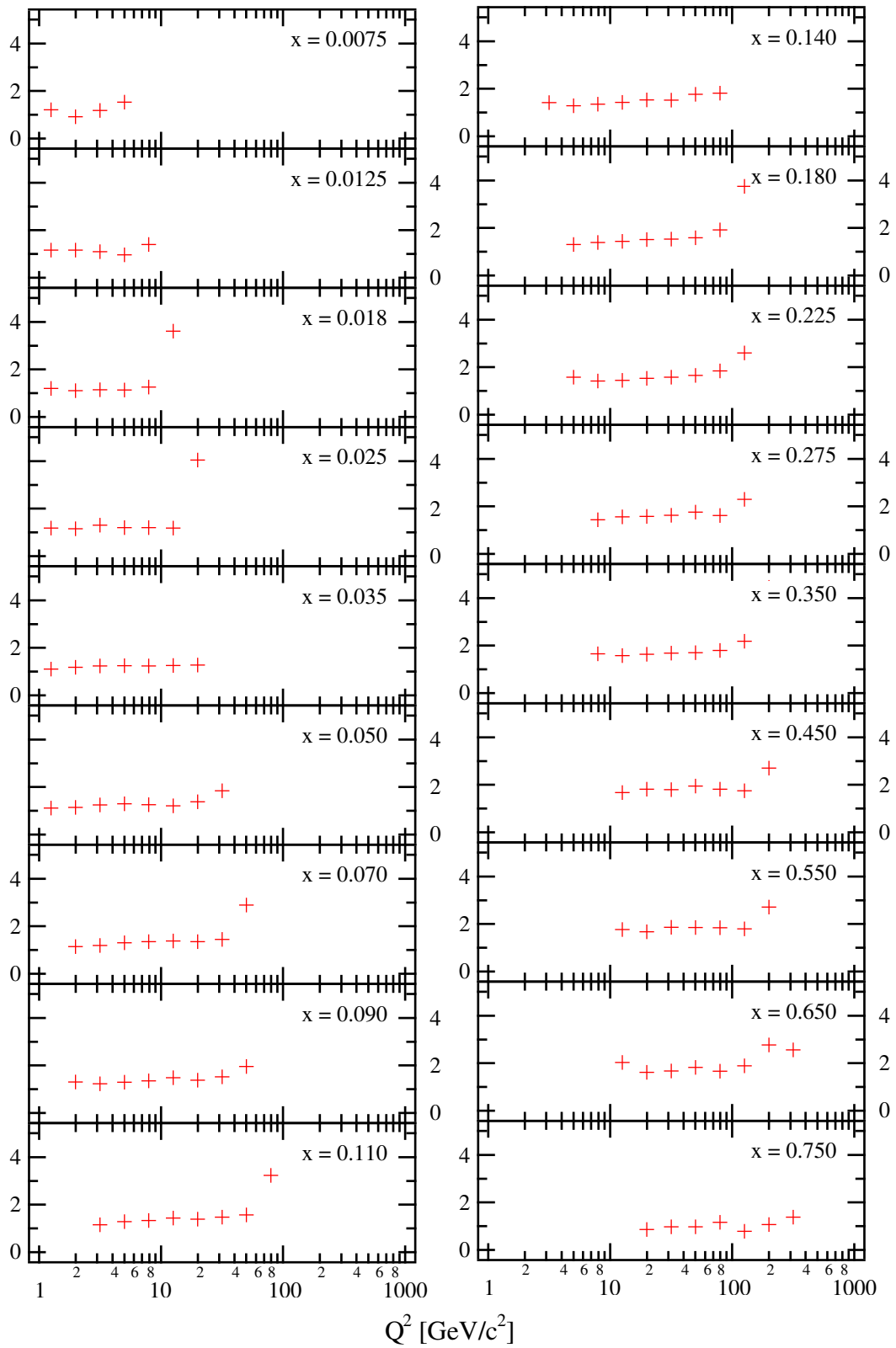

Figure 6.7: The total corrections applied to anti-neutrino events in the structure-function analysis.

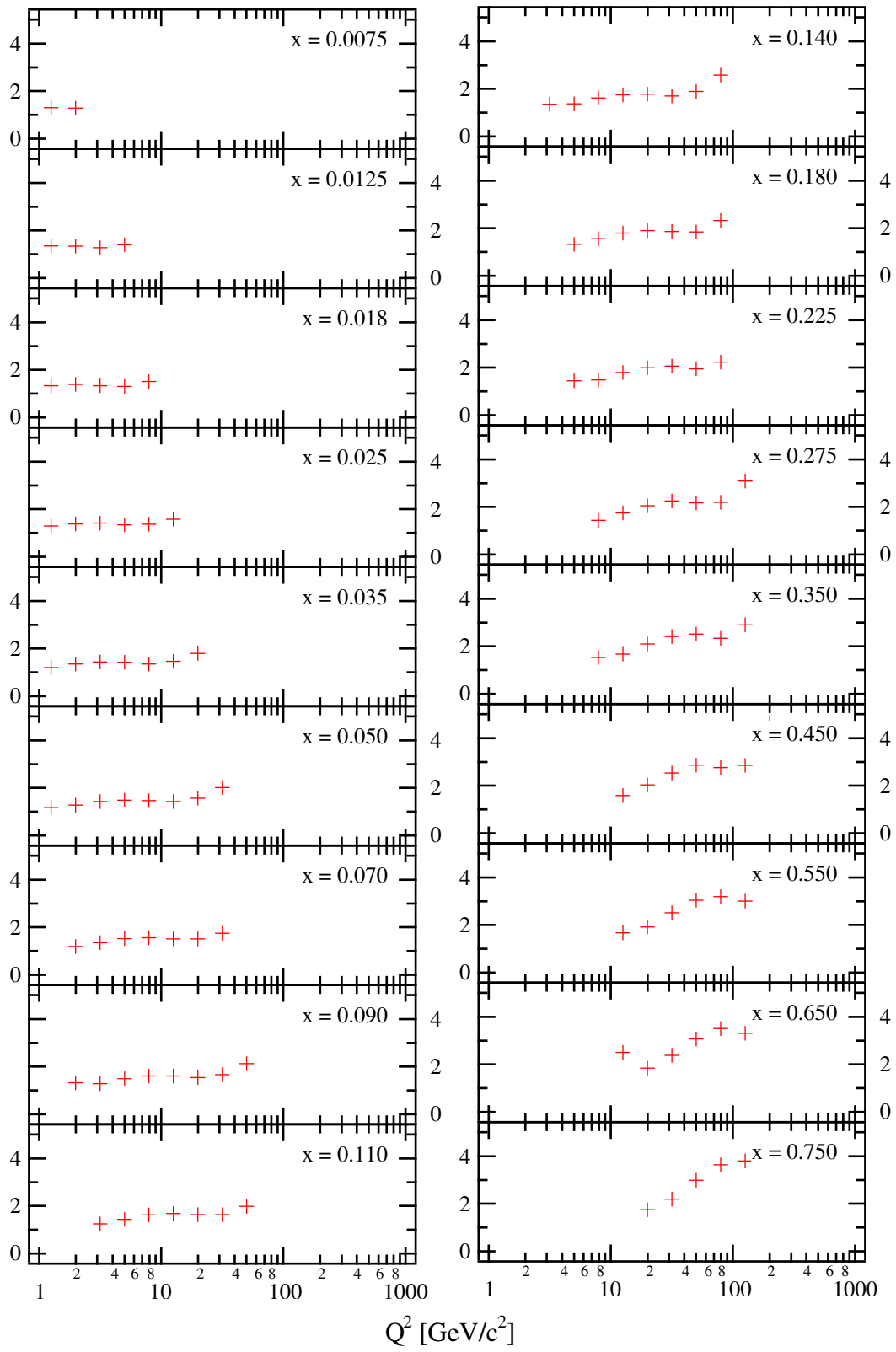

Figure 6.8: The acceptance corrections for neutrino events in the structure-function analysis.

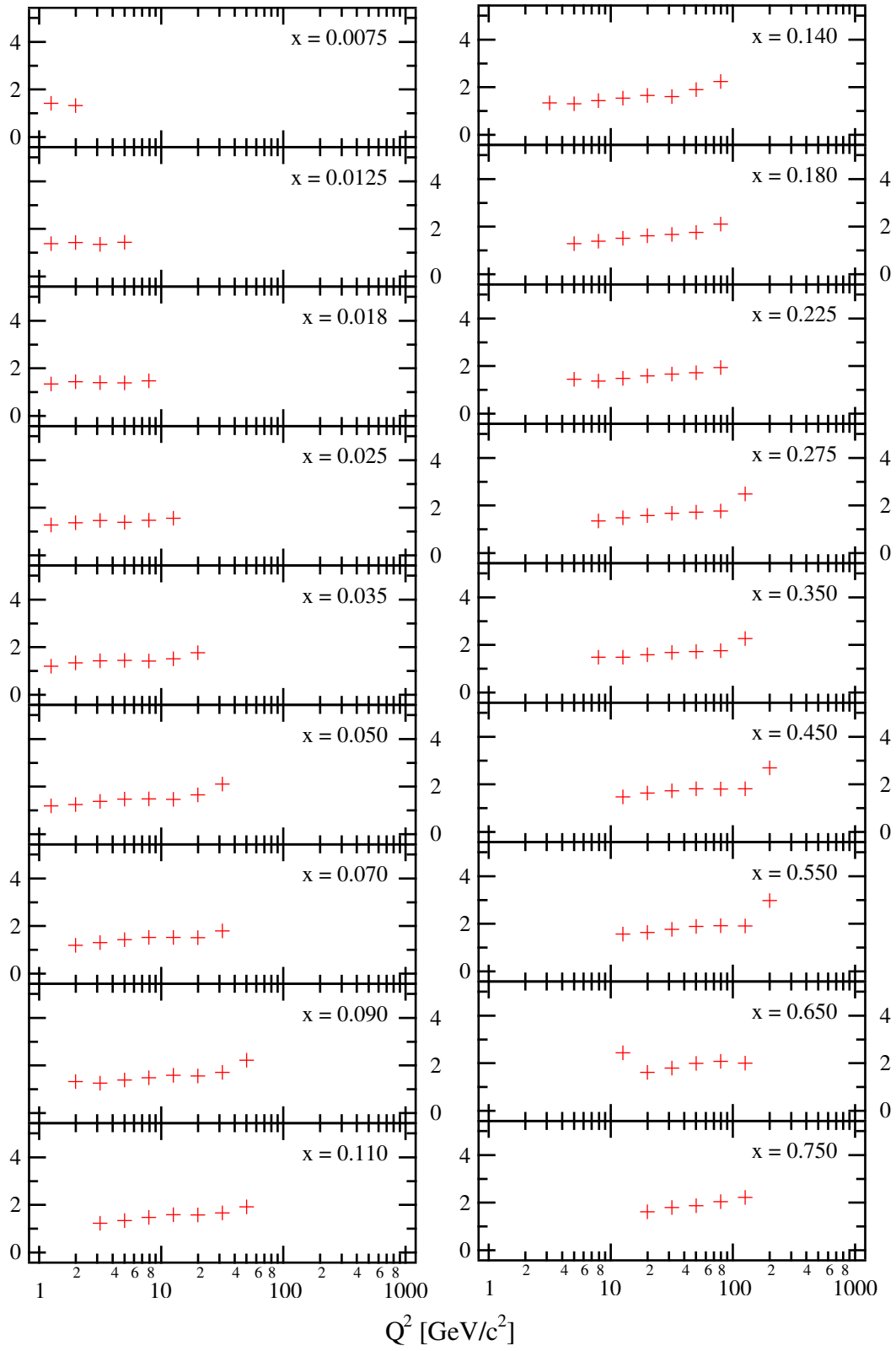

Figure 6.9: The acceptance corrections for anti-neutrino events in the structure-function analysis.

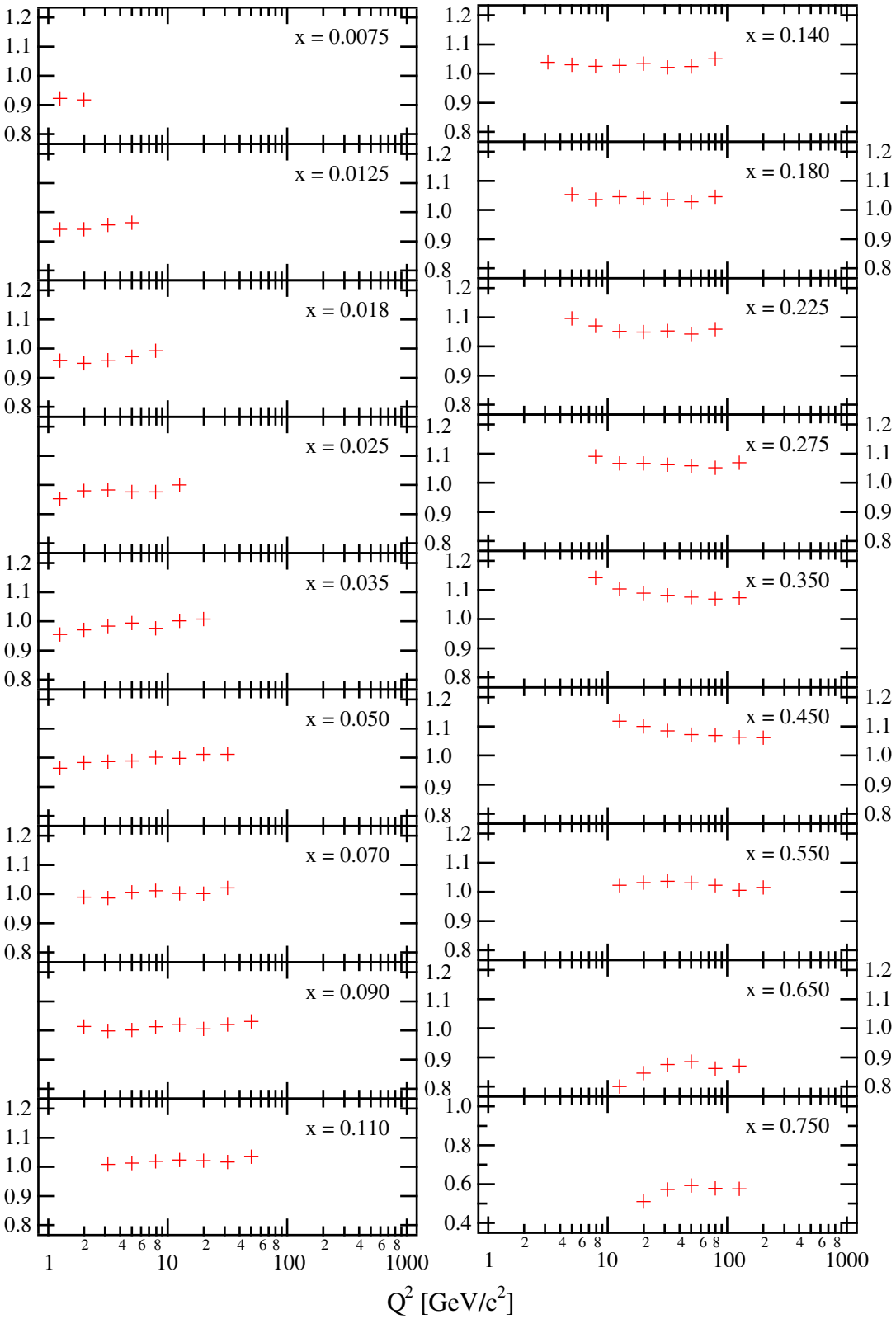

Figure 6.10: The smearing corrections for neutrino events in the structure-function analysis.

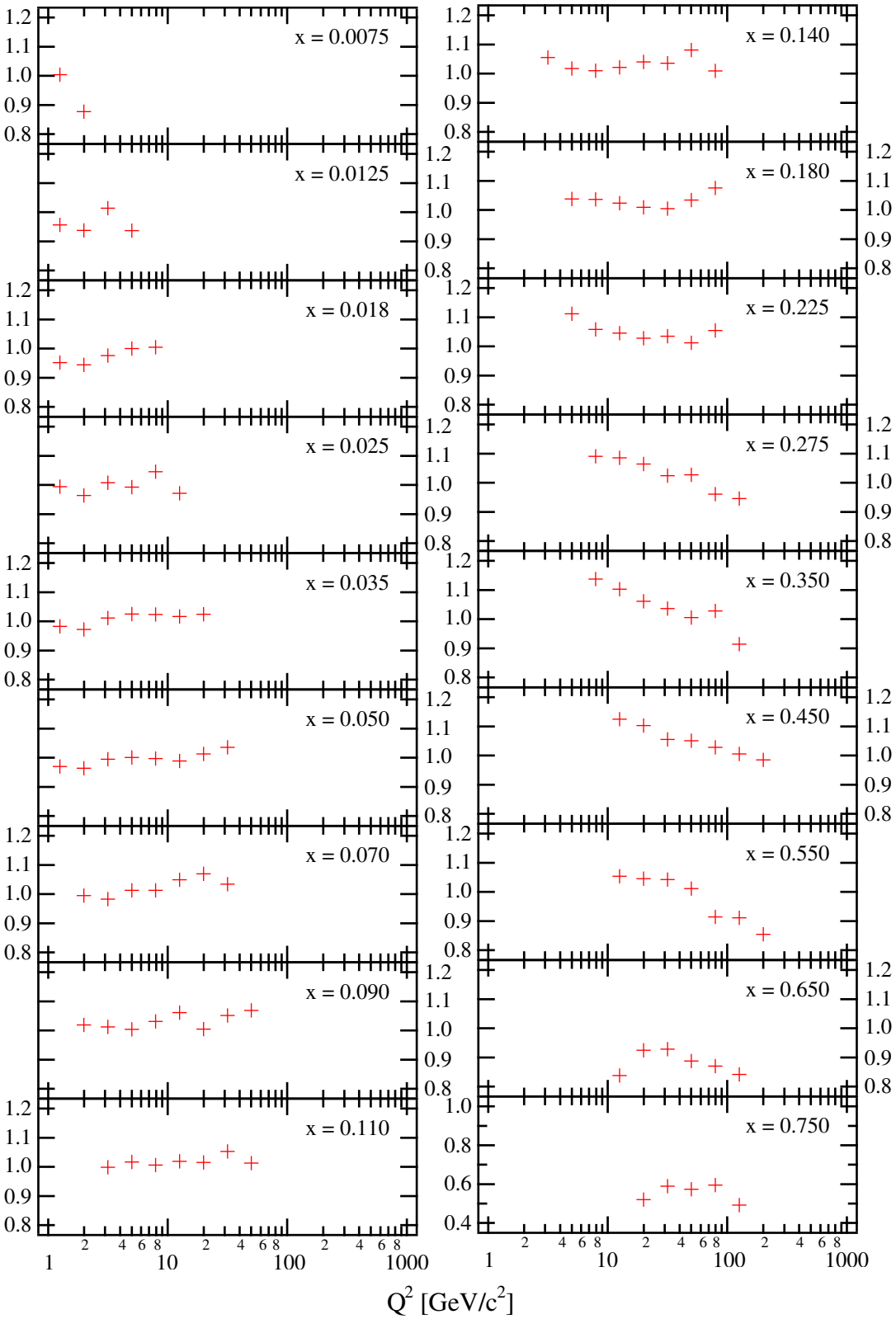

Figure 6.11: The smearing corrections for anti-neutrino events in the structure-function analysis.

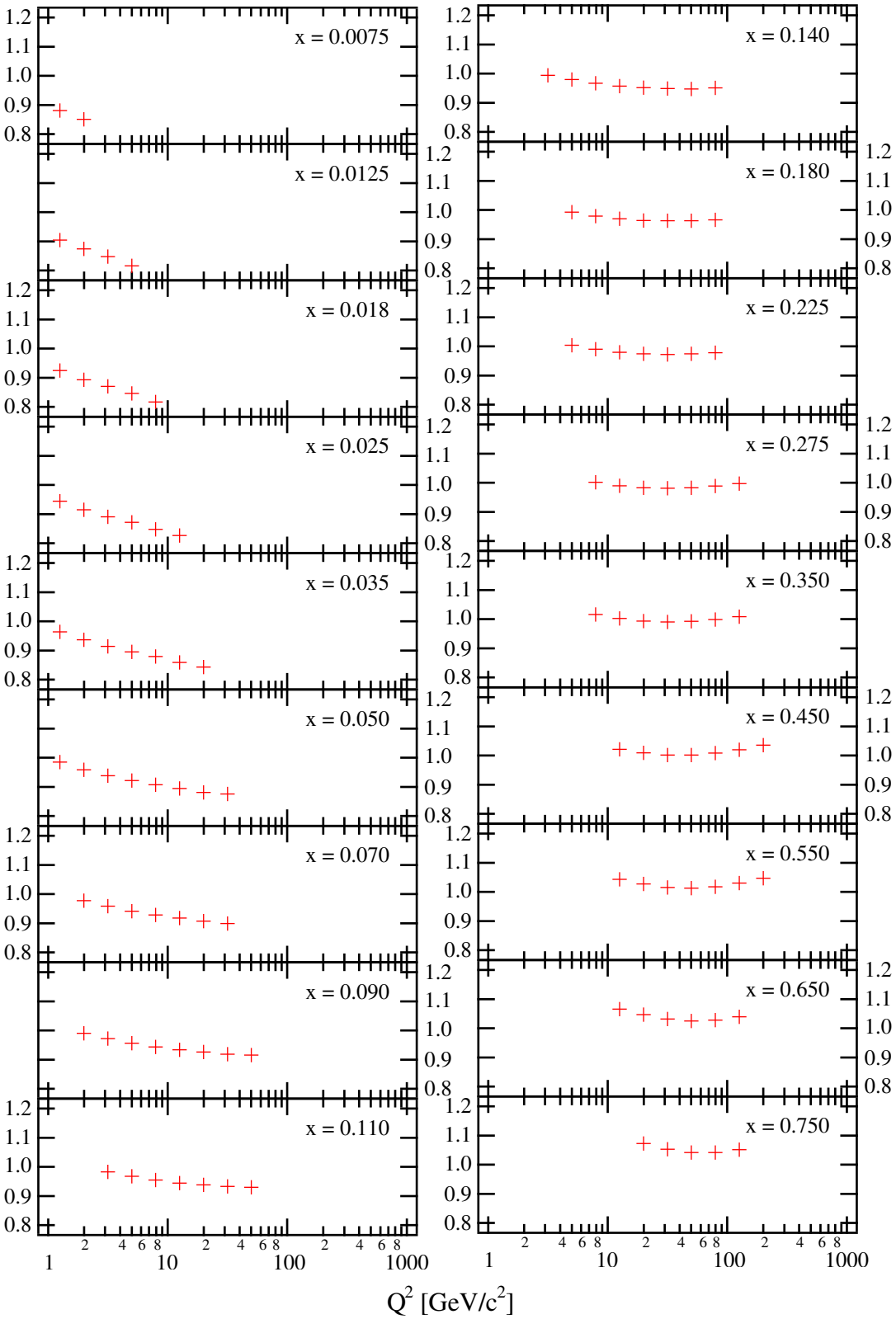

Figure 6.12: The physics-model corrections for neutrino events in the structure-function analysis.

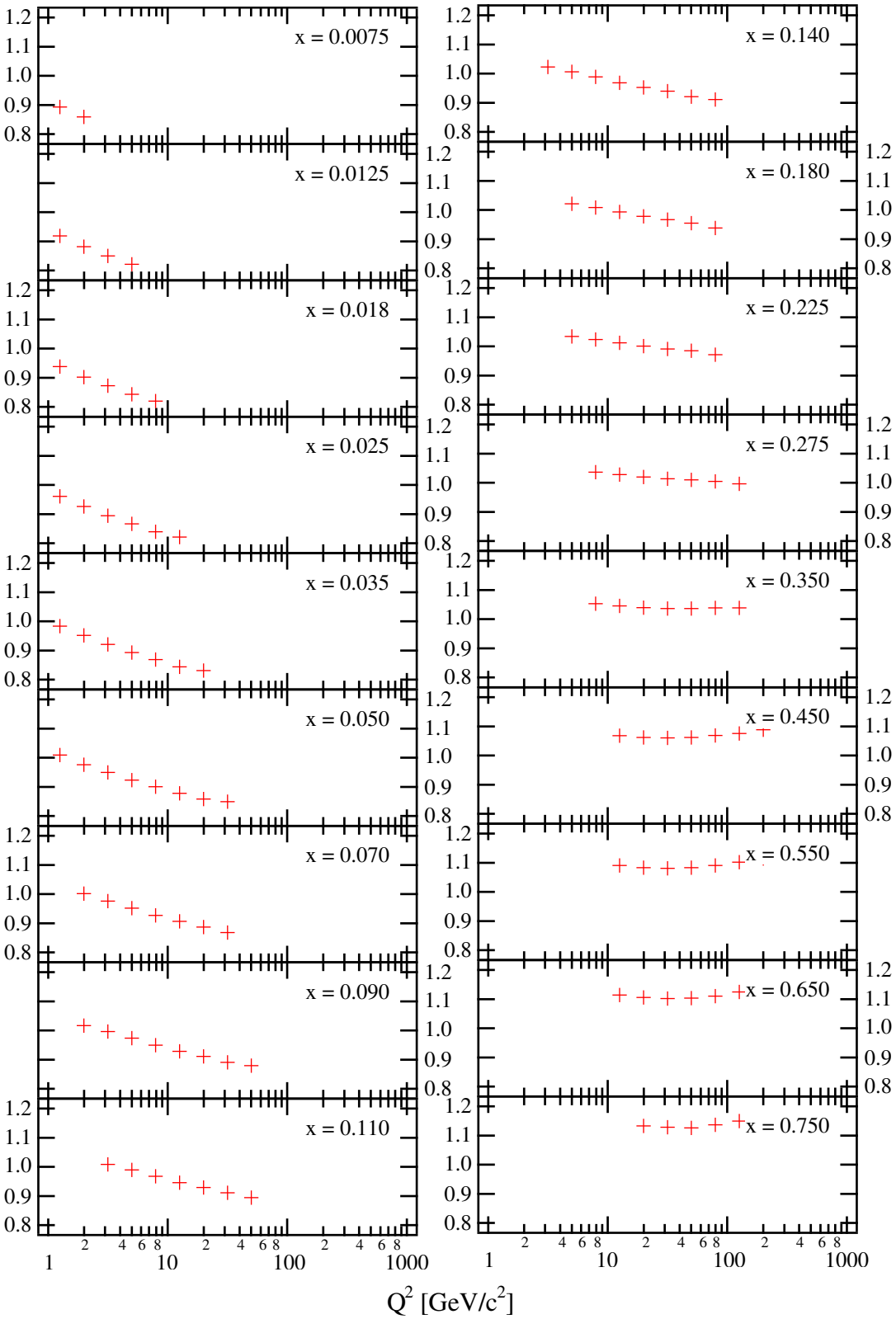

Figure 6.13: The physics-model corrections for anti-neutrino events in the structure-function analysis.

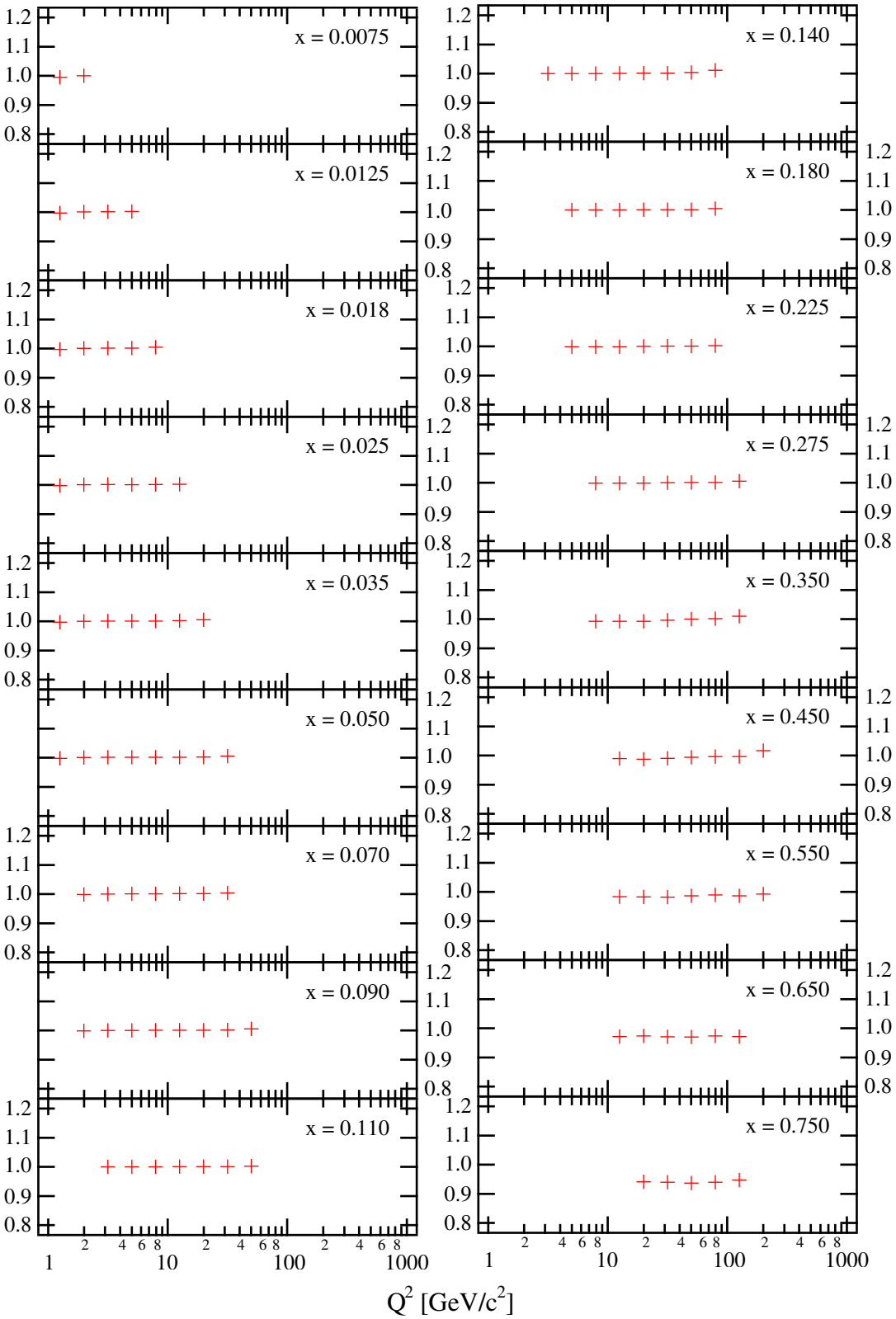

Figure 6.14: The bin-center corrections for neutrino events in the structure-function analysis.

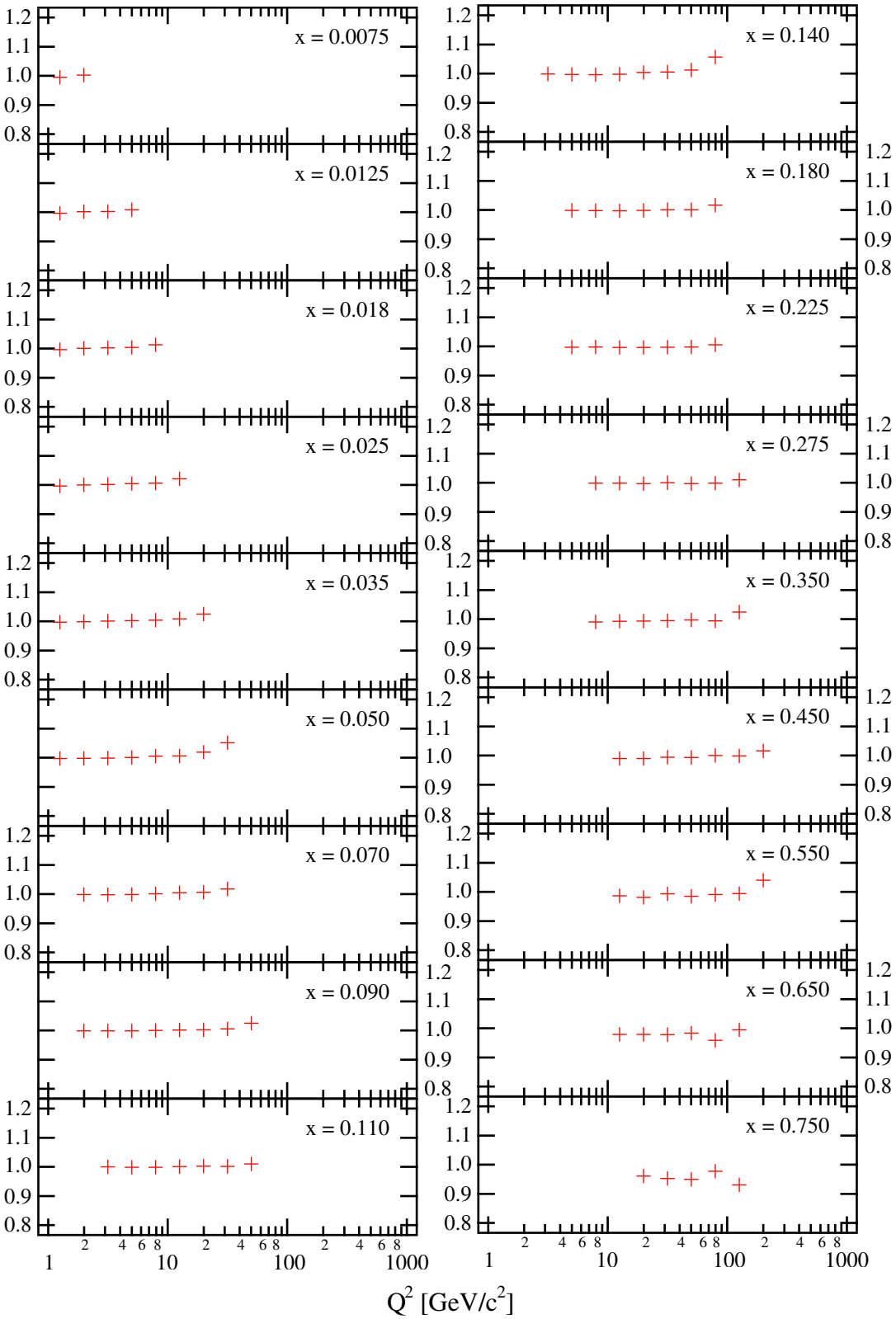

Figure 6.15: The bin-center corrections for anti-neutrino events in the structure-function analysis.

6.2.3 Combining Experiments

The structure functions F_2 and xF_3, and their associated statistical errors ΔF_2, ΔxF_3, and $\Delta F_2 \Delta xF_3$, are extracted separately for each experiment, E744 and E770, according to Equation 6.9. The structure functions are combined using the following procedure, which correctly incorporates the correlated statistical errors:

Define the structure-function vector

$$\vec{\mathbf{F}} = \begin{pmatrix} F_2 \\ xF_3 \end{pmatrix} \tag{6.23}$$

and the structure-function error matrix

$$\hat{\mathbf{V}} = \begin{pmatrix} \left(\Delta F_2\right)^2 & \Delta F_2 \Delta xF_3 \\ \Delta F_2 \Delta xF_3 & \left(\Delta xF_3\right)^2 \end{pmatrix} \tag{6.24}$$

Then to combine the vectors $\vec{\mathbf{F}}_{\text{E744}}$ and $\vec{\mathbf{F}}_{\text{E770}}$, and the matrices $\hat{\mathbf{V}}_{\text{E744}}$ and $\hat{\mathbf{V}}_{\text{E770}}$, the relations are:

$$\left(\hat{\mathbf{V}}_{\text{Combined}}\right)^{-1} = \left(\hat{\mathbf{V}}_{\text{E744}}\right)^{-1} + \left(\hat{\mathbf{V}}_{\text{E770}}\right)^{-1} \tag{6.25}$$

$$\left(\hat{\mathbf{V}}_{\text{Combined}}\right)^{-1} \vec{\mathbf{F}}_{\text{Combined}} = \left(\hat{\mathbf{V}}_{\text{E744}}\right)^{-1} \vec{\mathbf{F}}_{\text{E744}} + \left(\hat{\mathbf{V}}_{\text{E770}}\right)^{-1} \vec{\mathbf{F}}_{\text{E770}} \tag{6.26}$$

As a check, it can be noted that if $\Delta F_2 \Delta xF_3 = 0$ for both experiments, Equations 6.25 and 6.26 reduce to

$$\sigma^2_{A+B} = 1 \Big/ \left(1 \Big/ \sigma^2_A + 1 \Big/ \sigma^2_B\right) \tag{6.27}$$

and

$$f_{A+B} = \left(f_A / \sigma_A^2 + f_B / \sigma_B^2 \right) \Big/ \left(1/\sigma_A^2 + 1/\sigma_B^2 \right) \tag{6.28}$$

which are the familiar expressions for summing the results of two independent measurements.

6.3 Iteration

In both the flux and structure-function analysis, the physics-model correction requires a set of parton distributions based on some set of structure functions, and the Monte-Carlo correction requires a flux to calculate the smearing corrections. Since an input set of flux and structure functions is needed to extract a new output set of flux and structure functions, an iterative approach must be used. The steps of the "iterative loop" associated with this analysis are:

1) Assume a flux Φ_{EST} and a set of parton distributions q_{EST}.

2) Generate Monte Carlo events using q_{EST} and Φ_{EST}.

3) Apply the resolution smearing of section 4.1 to the events from step (2).

4) Use the Monte Carlo events from steps (2) and (3) to correct the low-E_{HAD} events and extract a flux Φ_{NEW} as discussed in chapter 5.

5) Use the events of step (2), but re-weight the events from Φ_{EST} to Φ_{NEW} as discussed in section 4.1.4.1, and apply the resolution smearing.

6) Use the Monte-Carlo events of step (5) to extract a set of structure functions F_{NEW}.

7) Fit a set of parton distributions q_{NEW} to the structure functions F_{NEW} using the physics-model parameterization described in section 4.2.

8) Replace $q_{NEW} \rightarrow q_{EST}$ and $\Phi_{NEW} \rightarrow \Phi_{EST}$ and repeat steps (1) through (7) until the difference between F_{NEW} and F_{EST} (from the previous iteration) is small.

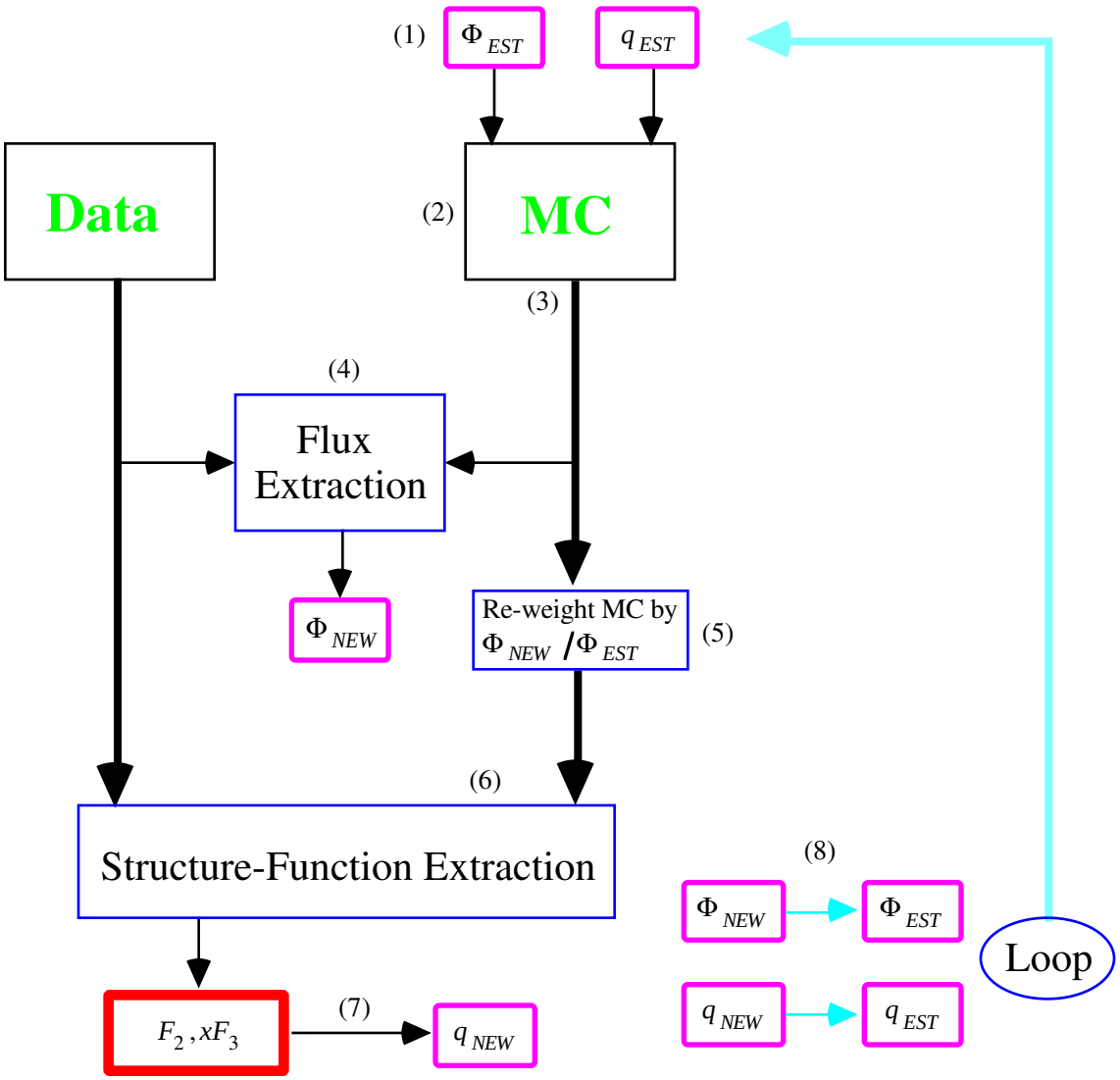

Figure 6.16: Diagram of the iterative analysis procedure. The numbers in parentheses correspond to the steps in the iteration described above.

In practice, the results converge after three iterations of steps (1) through (8). Figure 6.16 shows the iterative analysis loop in a diagrammatic form.

The structure-function extraction procedure was verified by generating a set of "fake data" events using the Monte Carlo, then using the "fake data" events in place of the data in the iterative loop. The resultant structure functions were identical to the structure functions used as input to the Monte Carlo.

6.4 Systematic Errors

This section contains the complete list of systematic errors identified in this analysis. Some of them have been described in earlier sections of this thesis, but all are included in the following sub-sections. The point-to-point systematic errors in Appendix D were generated by the following procedure:

• Vary the systematic quantity by the error listed (denoted as a shift of the systematic quantity by $1\delta_k$). With the exceptions noted below, each systematic quantity was varied by $\pm 1\,\delta_k$; that is, the error was calculated for both a positive and negative systematic shift.

• Use the Monte Carlo file created in step (2) of the iterative loop described in Section 6.3. The file used was the same as that used in the last iteration of the loop that resulted in the final structure functions.

• The parton distributions q_{EST} used for the systematic-error extraction were the same as were used as input to the last iteration of the final extraction loop; any exceptions are noted below.

• If was it was not necessary to extract a new flux, the same Φ as used in the last iteration for the final results was also used for the systematic variation.

• Steps (4) through (6) of the analysis described in Section 6.3 were performed, resulting in a flux Φ_k and associated structure functions F_k corresponding to this systematic variation.

• Within each (x, Q^2) bin, the systematic error reported in Tables D.2-D.9 is

$$\frac{\left(F_k(1\delta) - F\right)}{\left|\left(F_k(1\delta) - F\right)\right|} \times \frac{\left|\left(F_k(1\delta) - F\right)\right| + \left|\left(F_k(-1\delta) - F\right)\right|}{2} \tag{6.29}$$

That is, the shift in the table is the magnitude of average of the positive and negative shift, multiplied by the sign of the positive shift.

All of the systematic errors listed below are included in the "global systematic QCD fit" described in chapter 7.

6.4.1 Experimental Systematics

These errors are associated with systematic effects in the data analysis described in chapter 3.

Hadron energy calibration (C_{HAD}^{744}, C_{HAD}^{770}): As described in section 3.1.4, the hadron energy calibration for the experiment is known to within 1%. Due to the aging of the scintillator oil in the target counters, the re-adjustment of the photomultiplier-tube voltages, and changes made in the ADC readout electronics, the calibration of each of the two experiments E744 and E770 is allowed to be independently shifted by ±1%.

E_{HAD} shift (ΔE_{HAD}): As noted in section 3.1.4, there is a disagreement in the model of the hadron energy in the Monte Carlo and the data, and the data is corrected for this difference. The error in this correction is conservatively estimated to be ±100 *MeV*.

Muon energy calibration (C_μ): As described in section 3.2, the muon energy calibration for the experiment is known to within 1%. Since the same toroid spectrometer was used for both experiments E744 and E770, the same muon calibration constant is assumed for both experiments.

E_μ shift (ΔE_μ): The model of the systematic error for the E_{HAD} calibration is $C_{HAD} \times E_{HAD} + \Delta E_{HAD}$. To be consistent, the model of the systematic error in the E_μ calibration is taken to be $C_\mu \times E_\mu + \Delta E_\mu$. The shift in E_μ is therefore zero, with an assumed error ΔE_μ of ±100 *MeV*.‡

6.4.2 Flux-Extraction Systematics

B/A for neutrinos and anti-neutrinos ($(B/A)^{\nu,\bar{\nu}}_{\text{E744,E770}}$): As discussed in section 5.1.2.1, there is a statistical error from the flux extraction in the value of *B/A* which affects the flux. The errors in $(B/A)^{\nu}$ and $(B/A)^{\bar{\nu}}$ from experiments E744 and E770 are treated as separate systematic errors.

---

‡ A study was done assuming a quadratic term in the energy calibration, i.e., $E_{meas} = \Delta E + CE(1 + C'E)$. The quadratic coefficient C' was allowed to vary by ±2.5%/(200 *GeV*), the limit allowed by the hadron energy studies in [Sak90]. This study was performed separately for both the muon and hadron energy calibration, and the result in both cases was that the effect on the values of the structure functions was less than 10% of the shift due to ΔE.

Flux adjustment ($\Phi^{adjusted}$): As discussed in section 5.3.3, the difference between the actual flux extracted and the flux adjusted for a linear cross-section is treated as a systematic error. There is no "-1δ" shift for this error; the error in Tables D.4 and D.5 is the difference between the structure function extracted with $\Phi^{original}$ and the base structure function.

6.4.3 Cross-section Systematics

The following systematic errors come from errors in the ν-Fe cross-section.

Cross-section normalization (σ^{ν}/E): As discussed in section 5.3.1, there is an error of 2.1% in the world average of the neutrino-iron cross-sections. This systematic error results in a shift of ±2.1% in the level of the structure functions. There is no need to re-extract the flux for a shift in σ^{ν}/E since this does not change the relative flux.

Cross-section ratio ($\sigma^{\bar{\nu}}/\sigma^{\nu}$): As discussed in section 5.3.1, there is an error in the world average $\sigma^{\bar{\nu}}/\sigma^{\nu}$. However, the error quoted in Table 5.6 includes all the systematic effects for our experiment. In the systematic error analysis a new flux Φ_k and associated $\left(\sigma^{\bar{\nu}}/\sigma^{\nu}\right)_k$ are generated for all the systematic errors. Including the complete error from Table 5.6 in the variation of $1\delta_k$ would over-estimate the error due to the $\sigma^{\bar{\nu}}/\sigma^{\nu}$ error. Therefore, the only errors included in the shift of $\delta\left(\sigma^{\bar{\nu}}/\sigma^{\nu}\right)$ are the statistical, low-ν extrapolation, and acceptance-correction errors listed in Table 5.6. The resulting value of $\delta\left(\sigma^{\bar{\nu}}/\sigma^{\nu}\right)$ is 1.4%. There is no need to re-extract the flux for the shift in $\sigma^{\bar{\nu}}/\sigma^{\nu}$, since it does not change the relative flux.

6.4.4 Model Systematics

The following systematic errors come from errors in quantities measured from other analyses than the analysis described in this thesis. Aside from the error in R_{World}, the remaining errors come from the dimuon analysis [Rab92]. All of the model systematic errors apply to the physics model described in Section 4.2. To perform the systematic error study, a new $\left(q_{EST}\right)_k$ is derived by fitting to the F_{EST} from the next-to-the-last analysis iteration, varying the fixed parameters of the model only by the quantity listed. A new Monte Carlo file is not generated, nor are events re-weighted to the new cross-section; this is assumed to be unnecessary because these systematic shifts are small and because of the rapid convergence of the analysis iteration loop.

R_{World} error (δR): An error of ±15% is assumed for the parameterization of R given in Ref. [Whi90b].

Mass of the charm quark (m_c): As reported in Ref. [Rab93], the value of m_c is 1.31 ± 0.24. Thus the variation $\delta\left(m_c\right)$ is 18%.

Strange sea shape (α): As reported in Ref. [Rab93], the value of α (as defined in Equation 6.17) is 2.50 ± 0.65. Thus the variation $\delta(\alpha)$ is 26%.

Strange sea normalization (κ): As reported in Ref. [Rab93], the value of κ (as defined in Equation 6.16) is 0.373 ± 0.046. Thus the variation $\delta(\kappa)$ is 12%.

Charm branching ratio (B_c): As reported in Ref. [Rab93], the value of B_c is 0.105 ± 0.007. Thus the variation of $\delta\left(B_c\right)$ is 7%. Note: B_c enters into the analysis only indirectly via the small dimuon correction described in Section 4.1.4.2.

In addition to the above (relatively small) systematic errors, there is a systematic error due to the choice of the functional form of the physics model used in the Monte Carlo, as described in Section 4.2.1.5.

6.5 Results

Figures 6.17 and 6.18 display the values of F_2 and xF_3, respectively, with each *x*-bin shown separately. Figures 6.19-6.22 display as many *x*-bins on the same scale as possible, along with the QCD fits described in Chapter 7. Figure 6.19 displays F_2 extracted from this experiment and Figure 6.20 shows the values for $x > 0.3$. Similarly, Figures 6.21 and 6.22 display the values of xF_3 and the high-*x* values of xF_3. Only the statistical errors are shown. These Figures dramatically show the effects of scaling violations. True scaling would imply that the slopes of the lines connecting the data points be zero. Approximate scaling is only observed around $x = 0.14$.

Figure 6.24 shows F_2 and xF_3 at $Q^2 = 12.6\ GeV^2$, the average Q^2 of the data. Each structure function in this Figure was "averaged" over the Q^2 range of the experiment by fitting the data within each *x*-bin to a simple power-law form $F = A \times \left(Q^2\right)^C$, then evaluating the fit at $Q^2 = 12.6\ GeV^2$. Figure 6.25 shows the Q^2-averaged values for $\left(F_2 + xF_3\right)/2$ and $\left(F_2 - xF_3\right)/2$, which in the parton model are equivalent to $q(x)$ and $\bar{q}(x)$, the quark and anti-quark distributions respectively.

If the high-*x* structure functions are superimposed, as shown in Figures 6.23 and 6.24, it is clear that for $x > 0.5$ $F_2 \approx xF_3$. In Figure 6.25, it can be observed that $\bar{q}(x)$ is consistent with zero for $x > 0.5$. This observation will be addressed further in Chapter 7.

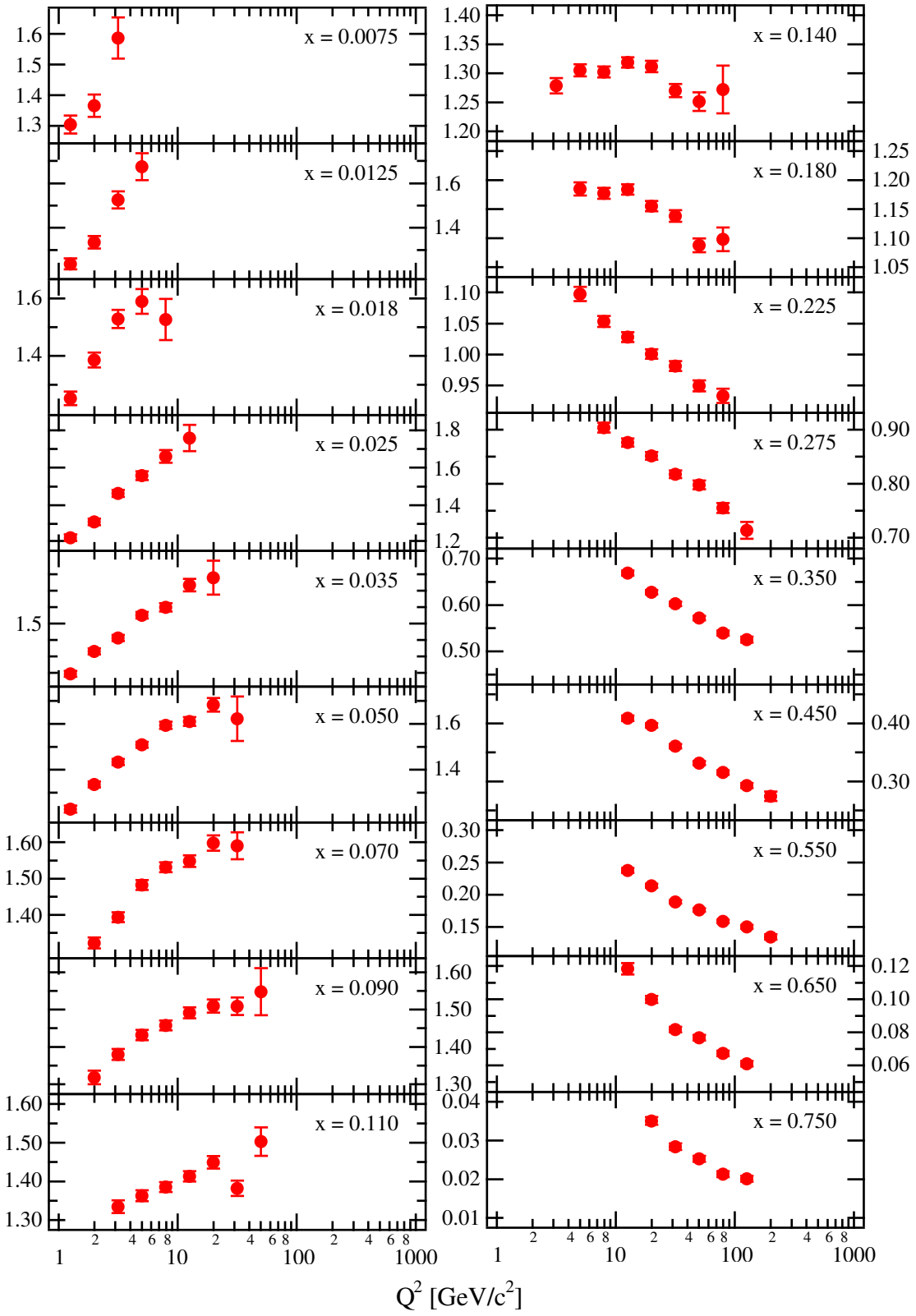

Figure 6.17: Structure function F_2. Each x-bin is displayed separately. Error bars are statistical only.

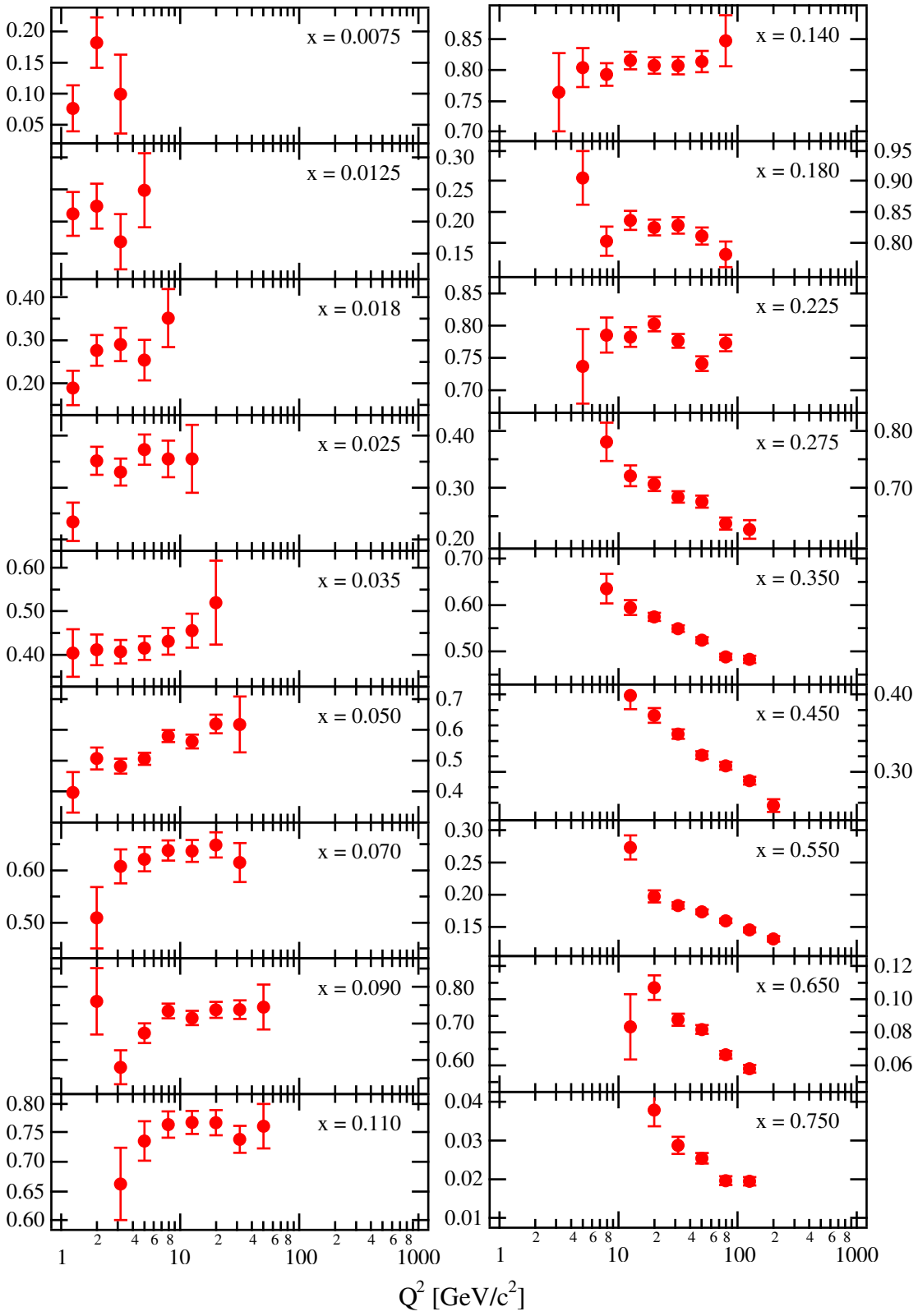

Figure 6.18: Structure function xF_3. Each x-bin is displayed separately. Error bars are statistical only.

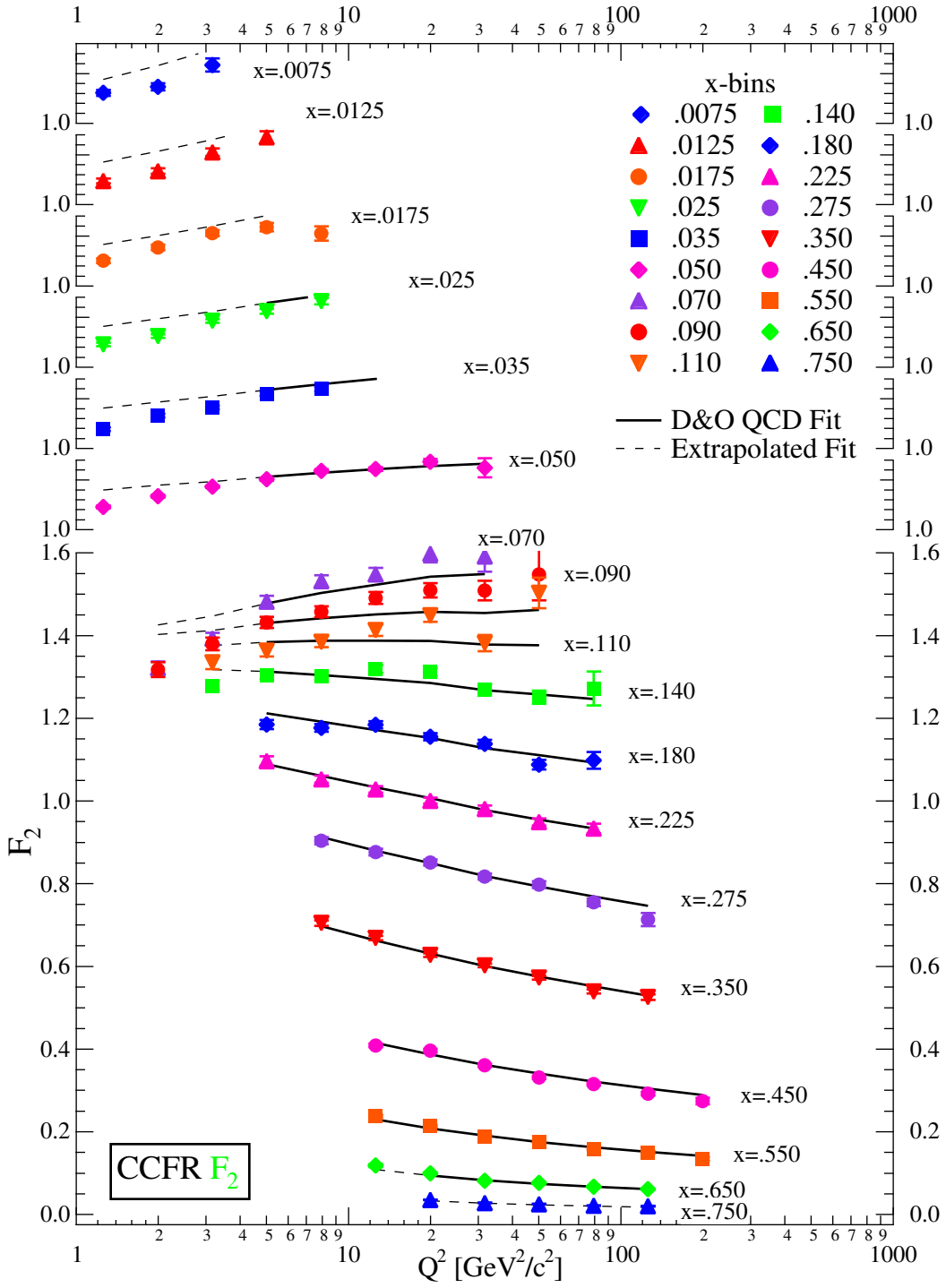

Figure 6.19: Structure function F_2, displaying as many x-bins as possible on a common axis. Error bars are statistical only. The solid lines are the QCD fit described in Chapter 7; the dashed lines extrapolate the fit to $Q^2 = 1 GeV^2$ and $x < 0.8$.

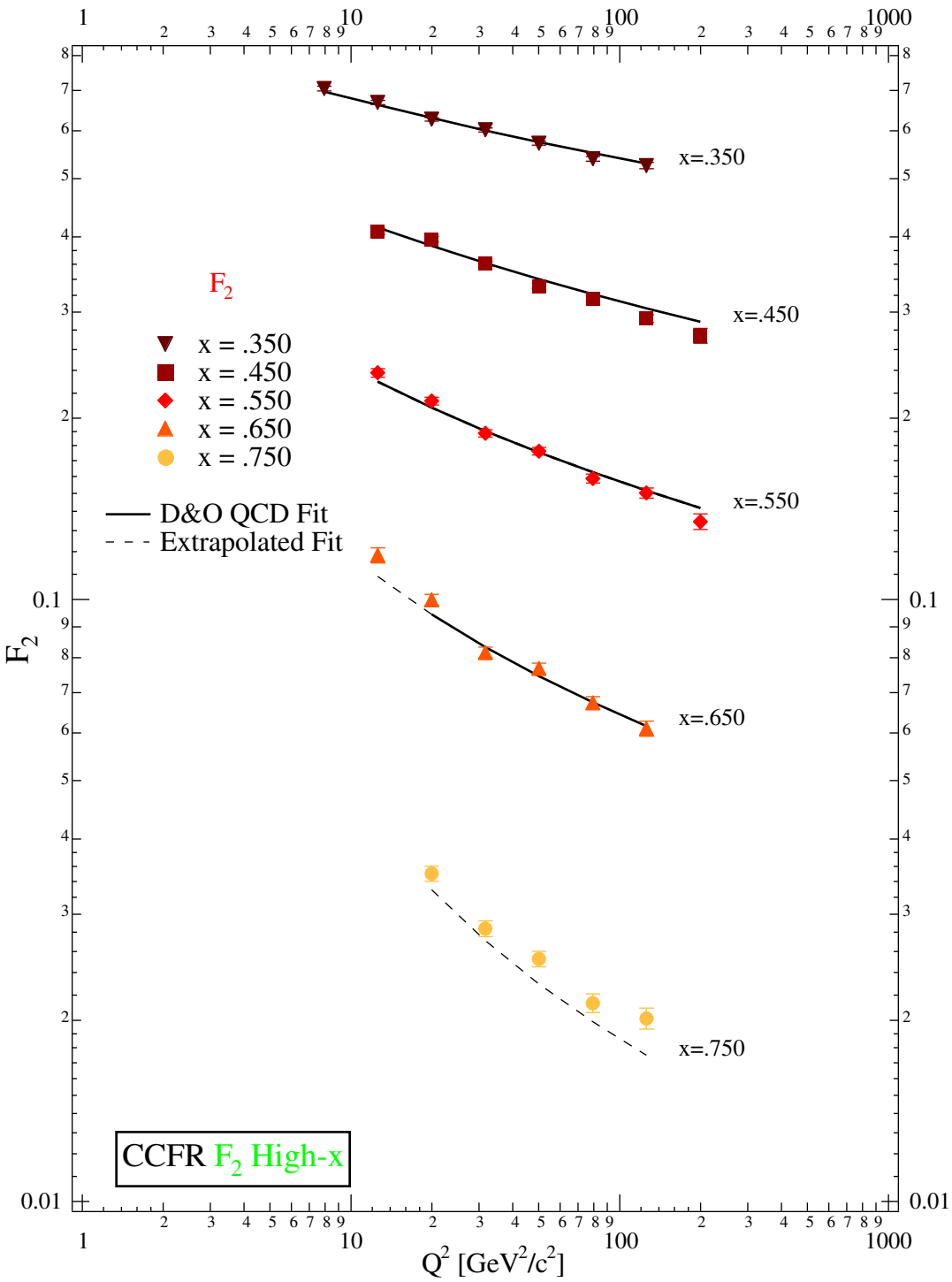

Figure 6.20: The high-x bins of structure function F_2. Error bars are statistical only. The solid lines are the QCD fit described in Chapter 7; the dashed lines extrapolate the fit to $Q^2 = 1 GeV^2$ and $x < 0.8$.

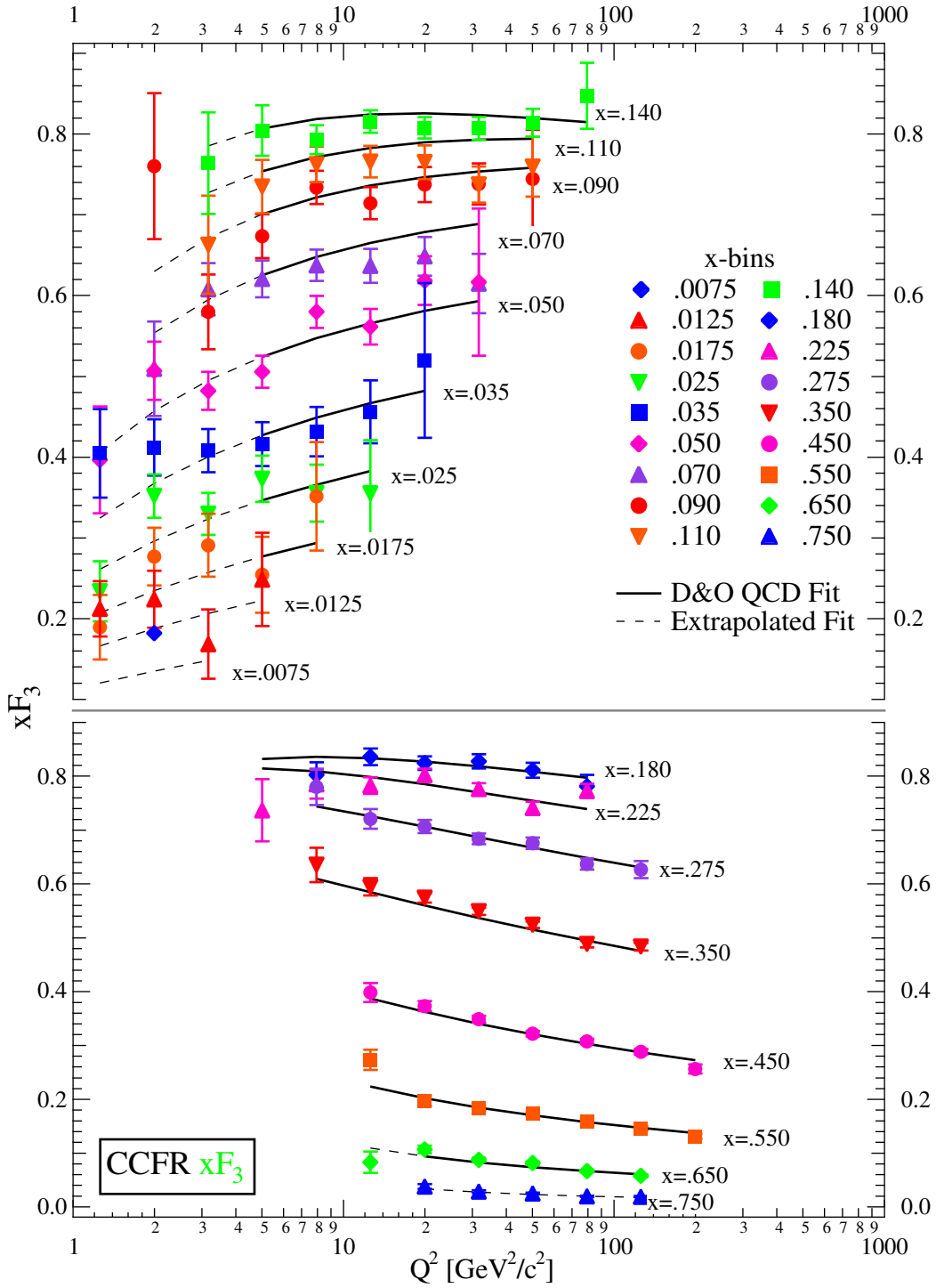

Figure 6.21: Structure function xF_3, displaying as many x-bins as possible on a common axis. Error bars are statistical only. The solid lines are the QCD fit described in Chapter 7; the dashed lines extrapolate the fit to $Q^2 = 1 GeV^2$ and $x < 0.8$.

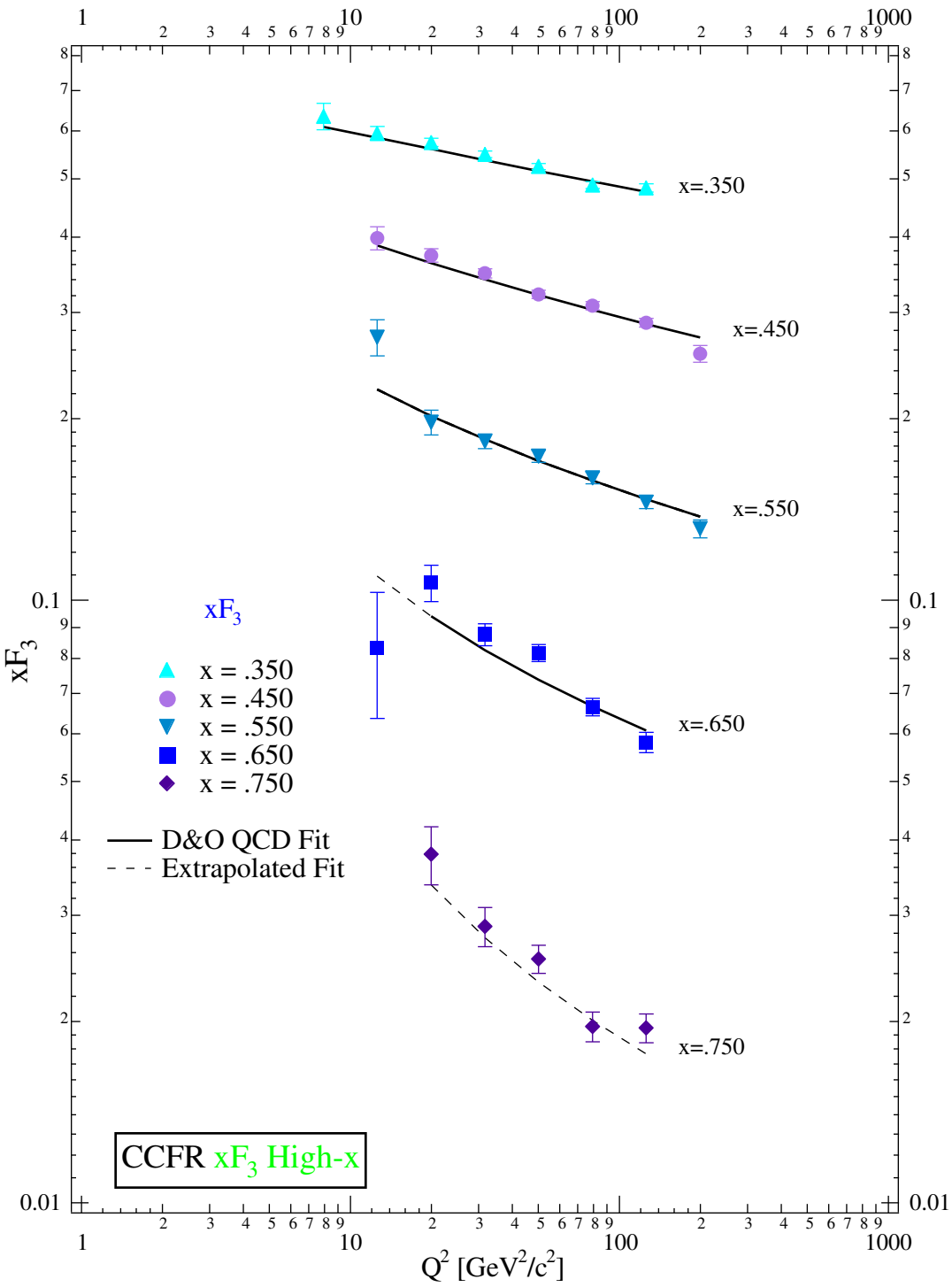

Figure 6.22: The high-x bins of structure function xF_3,. Error bars are statistical only. The solid lines are the QCD fit described in Chapter 7; the dashed lines extrapolate the fit to $Q^2 = 1 GeV^2$ and $x < 0.8$.

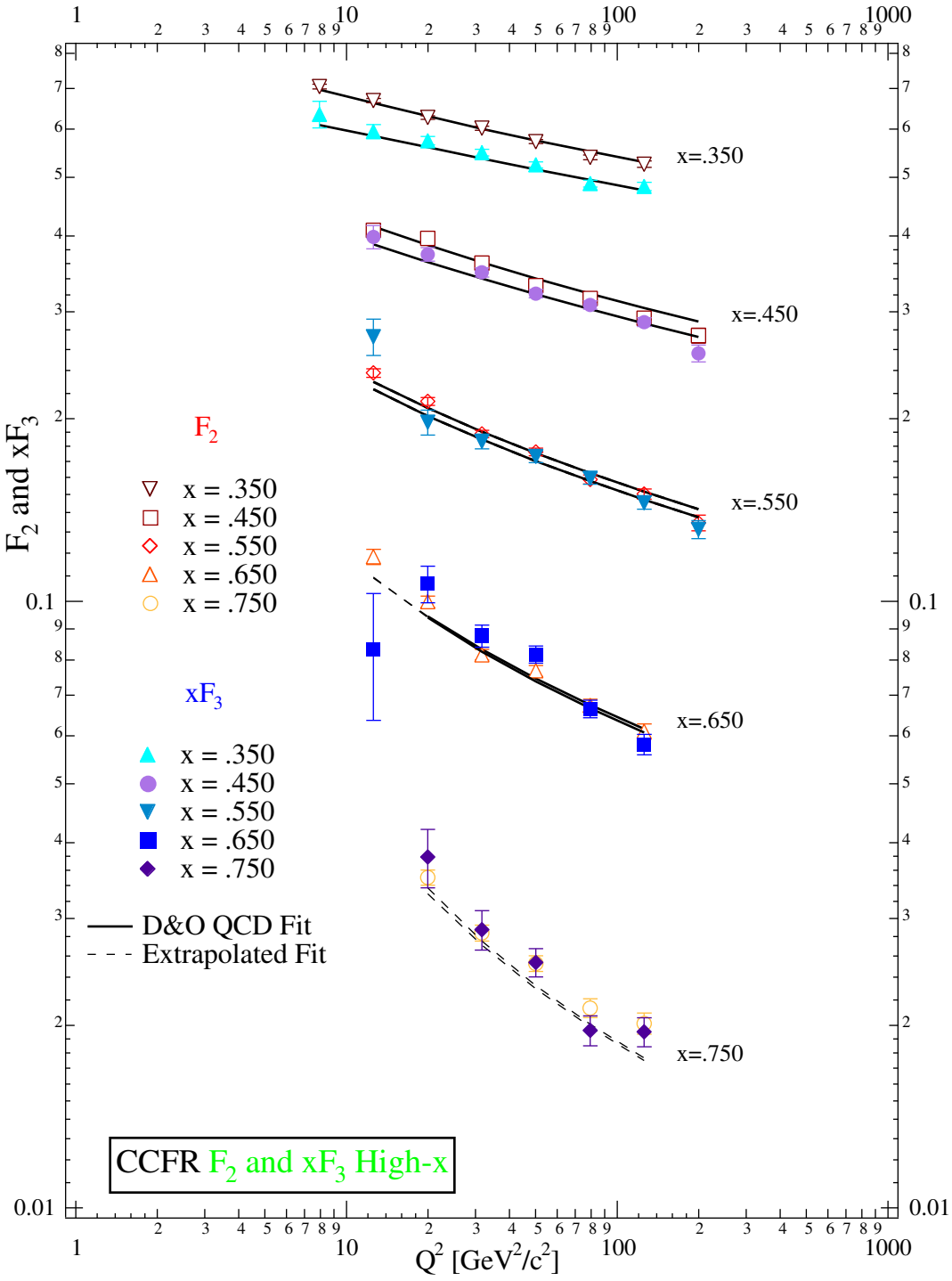

Figure 6.23: The high-x bins of structure functions F_2 and xF_3 superimposed to show $F_2(x>0.5) \approx xF_3(x>0.5)$. Error bars are statistical only. The solid lines are the QCD fit described in Chapter 7; the dashed lines extrapolate the fit to $Q^2 = 1 GeV^2$ and $x < 0.8$.

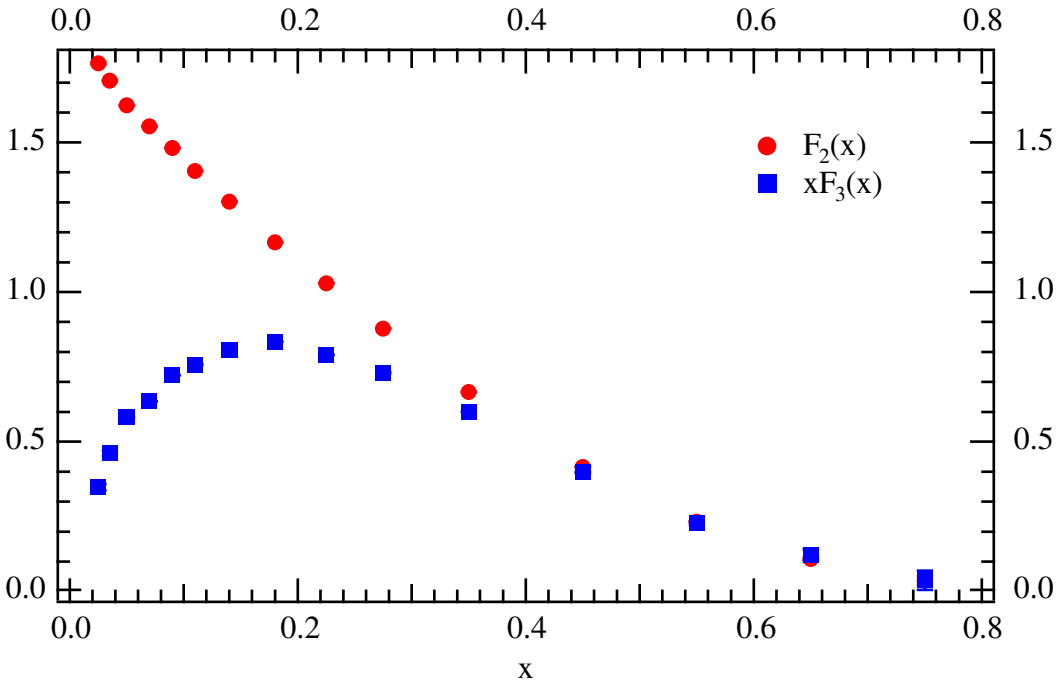

Figure 6.24: F_2 and xF_3 averaged at $Q^2 = 12.6\ GeV^2$.

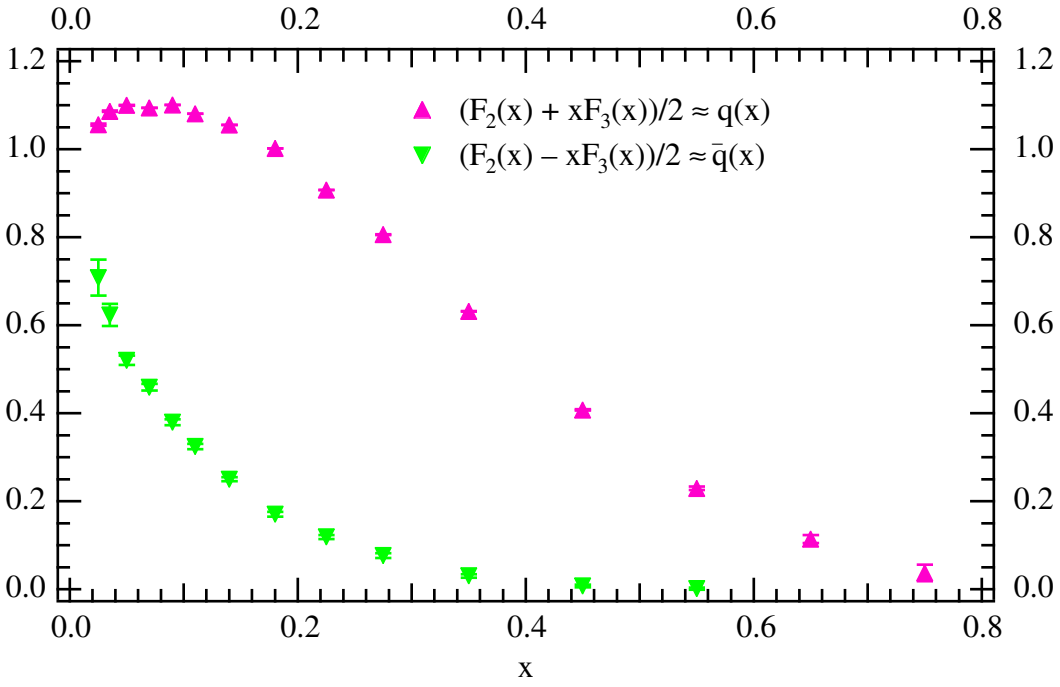

Figure 6.25: $\left(F_2 + xF_3\right)/2$ and $\left(F_2 - xF_3\right)/2$ averaged at $Q^2 = 12.6\ GeV^2$.